

RESEARCH ARTICLE | JUNE 09 2020

## Direct numerical simulation of multiscale flow physics of binary droplet collision

Xiaodong Chen (陈晓东)  ; Vigor Yang (杨威迦) 



*Physics of Fluids* 32, 062103 (2020)

<https://doi.org/10.1063/5.0006695>

 CHORUS



## Physics of Fluids

Special Topic:

John Michael Dealy (1937-2024): Celebrating His Life

Guest Editors: Alan Jeffrey Giacomini and Savvas G. Hatzikiriakos

[Submit Today!](#)

# Direct numerical simulation of multiscale flow physics of binary droplet collision

Cite as: Phys. Fluids 32, 062103 (2020); doi: 10.1063/5.0006695

Submitted: 5 March 2020 • Accepted: 10 May 2020 •

Published Online: 9 June 2020



Xiaodong Chen (陈晓东)<sup>1,a)</sup>  and Vigor Yang (杨威迦)<sup>2</sup> 

## AFFILIATIONS

<sup>1</sup>School of Aerospace Engineering, Beijing Institute of Technology, Beijing 100081, China

<sup>2</sup>School of Aerospace Engineering, Georgia Institute of Technology, Atlanta, Georgia 30332, USA

<sup>a)</sup> Author to whom correspondence should be addressed: [xiaodong.chen@bit.edu.cn](mailto:xiaodong.chen@bit.edu.cn)

## ABSTRACT

Direct numerical simulations are performed to investigate the multiscale flow physics of binary droplet collision over a wide range of Weber numbers and impact factors. All possible collision outcomes, including bouncing (both head-on and off-center), coalescence, reflexive separation, and stretching separation, are considered. The theoretical formulation is based on a complete set of conservation equations for both the liquid and gas phases. An improved volume-of-fluid technique, which is augmented by an adaptive mesh refinement algorithm, is used to track the liquid/gas interface. Several local refinement criteria are validated and employed to improve the computational accuracy and efficiency substantially. In particular, a thickness-based refinement technique is implemented for treating cases involving extremely thin gas films between droplets. The smallest numerical grid is  $\sim 10$  nm, which is on the order of  $10^{-5}$  times the initial droplet diameter. A photorealistic visualization technique is employed to gain direct insights into the detailed collision dynamics, including both the shape evolution and mass relocation. The numerical framework allows us to systematically investigate the underlying mechanisms and processes, such as gas-film drainage and energy and mass transfer, at scales sufficient to resolve the near-field dynamics during droplet collision. The nonmonotonic transition of bouncing and merging outcomes for head-on collision is identified by varying the Weber number over two orders of magnitude. A geometric relation defining the droplet interactions is developed. Analytical models are also established to predict the mass transfer between colliding droplets.

Published under license by AIP Publishing. <https://doi.org/10.1063/5.0006695>

## I. INTRODUCTION

Droplet collision is a basic fluid dynamics phenomenon observed in many natural and engineering environments, and it has been studied extensively over several decades. Much of the underlying physics of droplet collision, however, remain to be explored, especially at a resolution sufficient to quantify the key mechanisms and controlling parameters that dictate collision dynamics and ensured mass transfer between droplets.

The present study addresses the collision of two equal-sized droplets of the same liquid, as shown schematically in Fig. 1. The droplets move toward one another in parallel with equal velocity,  $U$ . The global process can be characterized by four parameters, which are defined as follows:

$$\text{Impact factor } B = X/D, \quad (1)$$

$$\text{Weber number } We = \rho_l U_r 2D/\sigma, \quad (2)$$

$$\text{Reynolds number } Re = \rho_l U_r D/\mu_l, \quad (3)$$

$$\text{Ohnesorge number } Oh = \mu_l/\sqrt{\rho_l \sigma D}, \quad (4)$$

where  $X$  is the distance between the centroids of the droplets in the direction perpendicular to the moving direction,  $D$  is the droplet diameter,  $\rho_l$  is the liquid density,  $U_r$  (equal to  $2U$ ) is the relative velocity,  $\sigma$  is the surface tension, and  $\mu_l$  is the liquid viscosity.

The outcomes of droplet collisions can be categorized into four different types: bouncing, coalescence, separation, and shattering.<sup>1</sup> Bouncing occurs when the relative velocity of the two droplets is not sufficiently high to overcome the resistance of the thin gas film between the impact surfaces. The recovery of deformed shapes causes a reverse motion to drive the droplets apart. Coalescence occurs when the two droplets contact and permanently merge into a single droplet. Separation is a temporary coalescence followed by the formation of liquid ligaments, which eventually break into two

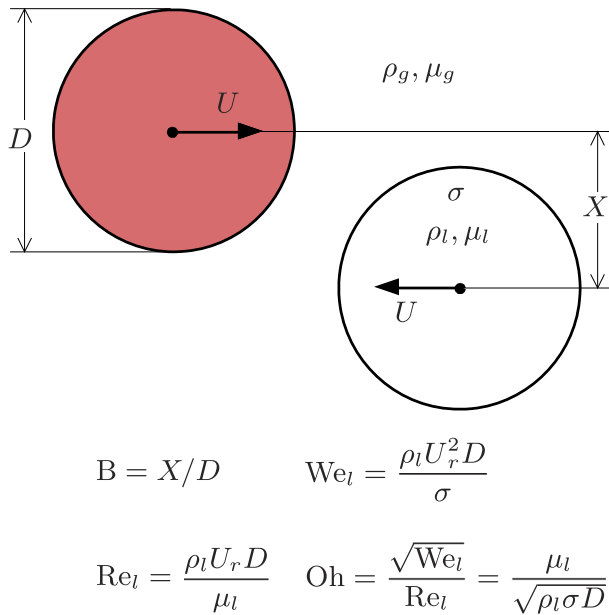


FIG. 1. Schematic diagram of binary droplet collision.

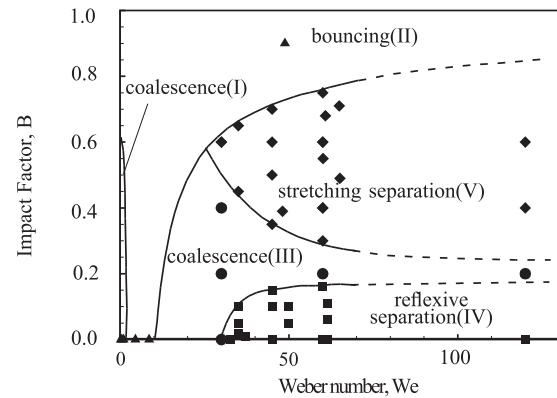


FIG. 2. Regime diagram of tetradecane droplet collision in nitrogen at  $P = 1$  atm in the  $We$ - $B$  coordinates. Symbols represent present simulation results:  $\blacktriangle$ , bouncing;  $\bullet$ , coalescence;  $\blacksquare$ , reflexive separation;  $\blacklozenge$ , stretching separation. The solid boundaries are adapted from Ref. 4 (Reproduced with permission from J. Qian and C. K. Law, "Regimes of coalescence and separation in droplet collision," *J. Fluid Mech.* **331**, 59 (1997). Copyright 1998 Cambridge University Press).

or more droplets. Shattering occurs under high-speed conditions when a thin liquid sheet is formed by the impact of the droplets.<sup>2,3</sup> Small droplets emerge from the sheet boundary during the development and recovery of the thin sheet. Shattering is not considered in the present study because it is dominated by a different control mechanism.<sup>1</sup>

A brief survey of the existing literature is presented as a starting point. Only the binary collision of equal-sized droplets of the same fluid is considered here. The establishment of the regime diagram<sup>4</sup> shown in Fig. 2 was of particular interest in early experimental investigations. Ashgriz and Poo<sup>1</sup> studied water droplet collision with the Weber number  $We$  and impact factor  $B$  over the ranges of 1–100 and 0–1, respectively. The mass transfer process was visualized by dyeing one droplet with a red colored medium. Both coalescence and separation were observed. The separation was further classified as reflexive or stretching. Reflexive separation occurs under near head-on conditions when the impact factor  $B$  is close to 0. The resulting droplet deformation gives rise to opposing internal flows that elongate the combined droplet, and it eventually causes the droplet to break apart. Stretching separation occurs under off-center conditions. The inertia of the noninteracting mass stretches the combined droplet until separation occurs. Ashgriz and Poo<sup>1</sup> developed theoretical (phenomenological) models for predicting reflexive and stretching separations; their results showed high consistency with the experimental data. This theory was later used by Ko and Ryou<sup>5</sup> and Munnannur and Reitz<sup>6</sup> to develop droplet collision models for spray simulations. Jiang *et al.*<sup>7</sup> experimentally studied the collision of equal-sized water and normal-alkane droplets with radii of  $\sim 150 \mu\text{m}$ . The dynamics of hydrocarbon droplets were found to be significantly richer than those of water droplets in terms of collision outcomes. Two additional regimes were observed, namely,

coalescence after minor deformation and bouncing. The outcome of a head-on collision varies from coalescence to bouncing and re-coalescence with increasing Weber numbers. The nonmonotonic variation was not observed for water droplets. By varying the density of the ambient gas, through either the pressure or the molecular weight of the gas, Qian and Law<sup>4</sup> confirmed that water droplet collision does exhibit nonmonotonic behaviors. The gas density was found to be a dominant parameter in the occurrence of coalescence upon collision. A phenomenological analysis was performed based on the study of Jiang *et al.*<sup>7</sup> Criteria for coalescence and separation during head-on collisions were established by considering the droplet kinetic energy (KE), surface energy (SE), and viscous dissipation.

The effect of the fluid properties, especially the liquid viscosity, on the droplet dynamics and the regime diagram has been studied extensively. Qian and Law<sup>4</sup> investigated regime diagrams of different liquid/gas systems experimentally using water and hydrocarbon droplets in air, nitrogen, helium, and ethylene. The pressure ranged from 0.6 atm to 12 atm. The coalescence of hydrocarbon droplets was found to be promoted in the presence of hydrocarbon vapor in the environment. Willis and Orme<sup>8</sup> conducted an experimental investigation of the binary droplet collision in a vacuum. The aerodynamic effect that tends to disrupt the collision process was eliminated. Dai and Schmidt<sup>9</sup> performed numerical simulations of head-on collisions using two equal-sized droplets with a three-dimensional (3-D) finite-volume method using moving meshes. The effect of the collision Reynolds number on the maximum deformation amplitude was examined. The results were consistent with the experimental observations by Willis and Orme.<sup>8</sup> The role of the viscosity became statistically insignificant in determining the maximum droplet deformation at sufficiently high Reynolds numbers. Gotaas *et al.*<sup>10</sup> studied, both experimentally and numerically, the influence of the viscosity on droplet collision under room conditions. The viscosity varied from 0.9 mPa s to 48 mPa s, and the

Weber numbers varied from 10 to 420. The boundary between coalescence and stretching separation shifted in higher Weber numbers with increasing viscosity. The absence of reflexive separation for small droplets and the shift of the stretching separation boundary were explained in terms of dissipation of collision kinetic energy in the combined droplet.

Krishnan and Loth<sup>11</sup> proposed empirical models for all the regime boundaries using available experimental data. The models account for the effects of ambient gas properties and include the boundary between coalescence after minor deformation and bouncing for the first time. However, it is notable that the database involves significant experimental uncertainties due to difficulties in characterizing the impact conditions and in controlling any precollision instabilities. Recently, Sommerfeld and Kuschel<sup>12</sup> performed an extensive experimental study on the binary droplet collision of various liquids over a wide range of viscosities, from 1 mPa s to 60 mPa s. They found that fluid viscosity plays an essential role in determining the intersection of bouncing, stretching separation, and coalescence in the regime diagram, as well as the transition from coalescence to separation for head-on collision. The models of both Ashgriz and Poo<sup>1</sup> and Jiang *et al.*<sup>7</sup> were employed to describe the boundaries between coalescence and stretching and reflexive separations. The lower boundary of bouncing can be reasonably described by the model by Estrade *et al.*<sup>13</sup> However, it requires further theoretical analysis and improvement.<sup>12</sup>

Theoretical studies were performed to understand the detailed droplet dynamic and ambient flow evolution such as the formation and drainage of the gas film between droplets. Roisman<sup>14</sup> investigated the initial stage of droplet motion that was dominated by the inertia force. The surface tension and viscous stress were also taken into account to provide a complete description. The work was further improved to yield more physically consistent results.<sup>15</sup> The dynamics of the lamella formed by droplet collision were explored. Universal dimensionless distributions for the lamellar thickness, velocity, and pressure were obtained. For low and moderate Weber and Reynolds numbers, the evolution of the lamella thickness appeared to be independent of the droplet viscosity and surface tension. The results also indicated the modeling limitation associated with the approximation of the lamella by a disk and the use of the energy balance approach. Zhang and Law<sup>16</sup> performed a theoretical analysis on head-on binary droplet collision in a gaseous environment with Weber numbers over a range of  $O(1)$ – $O(10)$ . A large deformation of the droplets and the gas-film drainage between the droplets were considered. The predicted nonmonotonic coalescence–bouncing–coalescence transition of hydrocarbon droplets at 1 atm showed good consistency with the experimental observations. The occurrences of bouncing for different liquids and ambient pressures were also examined.

A numerical simulation provides information that is difficult to measure and observe during experiments, especially for small-scale dynamics such as the near-field interaction of droplets before merging. Nobari *et al.*<sup>17</sup> simulated the head-on collision of equal-sized droplets using a front-tracking technique. When two droplets collide, a thin layer forms between the droplet surfaces. It is then artificially removed at a prescribed time to model the interfacial rupture. If no rupture occurs, the droplets rebound. If the film ruptures, the droplets coalesce, either permanently or temporarily,

and then, in some cases, they split. Although the predicted boundary between permanent and temporary coalescence was found to be consistent with the experimental observations, the exact boundary in the parameter space depended on the time of rupture. Pan *et al.*<sup>18</sup> investigated the head-on collision of binary droplets using a front-tracking method. The instant at which the interface between two impacting droplets ruptured was treated empirically as an input parameter. The energy budgets for bouncing and coalescence were examined. Since a certain area of the interface was artificially removed during droplet merging, the surface energy decreased abruptly after the rupture, rendering the total energy (TE) non-conserved.

In reality, droplets merge when they are brought together within a distance at which the van der Waals force prevails. To model this process from a multiscale point of view, Jiang and James<sup>19</sup> incorporated the van der Waals force into a volume-of-fluid (VOF) method to simulate the head-on droplet collision. Two different approaches were implemented. The first employed a body force that was computed as the negative gradient of the van der Waals potential; the second employed the van der Waals force in terms of a disjoining pressure in the film that was determined by the film thickness. The van der Waals force calculated from the two methods resulted in qualitatively similar effects on the coalescence. The disjoining pressure method was much less computationally intensive, but relied on the assumption of a small interfacial slope. The van der Waals force was overpredicted when the interface was convex and underpredicted when the interface was concave. Yoon *et al.*<sup>20</sup> introduced the van der Waals force into a boundary integral formulation using a disjoining pressure approximation. The dynamics of the gas film were successfully simulated with a numerical resolution of the film thickness of up to  $O(10^{-4})$  times the undeformed droplet radius, for the capillary number range of  $O(10^{-4})$  to  $10^{-1}$  and viscosity ratio of  $O(10^{-1})$  to 10). The results were qualitatively consistent with the experimental data on head-on collision with higher capillary numbers, but not with lower capillary numbers, where the gas film remained relatively spherical during the collision. The disjoining pressure provided a good leading-order approximation for relatively flat interfaces, but failed to capture the physics involved during the final stage of the gas-film rupture. This approximation for the van der Waals force is, thus, not sufficiently robust in predicting droplet merging.

To treat microscale effects in a fixed numerical grid system, subgrid models were recently developed for the gas-film evolution. For example, Kwakkel *et al.*<sup>21</sup> extended a multiple-marker coupled level-set/VOF approach, along with the use of the gas-film drainage model of Zhang and Law,<sup>16</sup> to estimate the total film drainage time prior to coalescence. The head-on collisions of two equal-sized droplets were predicted for Weber numbers of 2.3, 9.33, 13.63, and 61.4, corresponding to four different collision regimes. A good consistency with the experimental data was obtained. Rajkotwala *et al.*<sup>22</sup> incorporated the same gas-film drainage model into an improved local front-reconstruction framework. A qualitative match with the experimental observations was achieved, but generating a quantitatively accurate prediction of the gas-film drainage time remained a challenge.<sup>22</sup> A different gas-film drainage model was proposed by Mason *et al.*<sup>23</sup> based on a quasi-one-dimensional approach, which was then integrated with a VOF code by prescribing the velocity and thickness boundary conditions for the gas-film equation. Musehane

*et al.*<sup>24</sup> developed a more general gas-film model for droplet collision over a broad range of conditions, and it was not restricted to head-on collision of equal-sized droplets. The model was implemented in a multiple-marker VOF framework to study the droplet dynamics. This study led to the accurate prediction of interfacial deformation during droplet collision and the subsequent dynamics. The calculated collision outcomes consistently showed good agreement with the experimental data.<sup>24</sup> The calculated minimum gas-film thickness for the bouncing case also matched with that obtained from the direct numerical simulation using a thickness-based adaptive mesh refinement (AMR) technique.<sup>25</sup>

In addition to droplet merging, coalescence and separation have been studied extensively using various numerical methods. Inamura *et al.*<sup>26</sup> applied a lattice Boltzmann method to study binary droplet collision with a liquid/gas density ratio of 50. The predicted boundary between coalescence and separation was highly consistent with the other theoretical results. The mixing of the two colliding droplets was investigated by tracing the fluid particles in the droplets at a Weber number of  $\sim 80$ . Maximum mixing occurred at an impact factor of  $\sim 0.2$  in the reflexive separation regime. Pan and Suga<sup>27</sup> simulated binary droplet collision in various regimes using a level-set method. The results suggested that the bouncing mechanism was governed by macroscopic dynamics, but coalescence after minor deformation was related to microscopic dynamics. Sun *et al.*<sup>28</sup> studied binary droplet collision using a semi-implicit moving particle method. The mass transfer was characterized by tracking the particles, and the source of newly formed satellite droplets was identified. A mixing map in terms of droplet speed and impact number was established for Weber numbers over a 0–5 range. The mixing efficiency sharply decreased in the stretching separation regime in the direction away from the coalescence boundary. Finotello *et al.*<sup>29</sup> used a VOF method to study the effect of viscosity on the binary droplet collision for a wide range of impact conditions. The Weber number varied between 20 and 100, the impact parameter was between 0 and 0.8, and the capillary number was between 0.1 and 1. Three different collision outcomes (coalescence, stretching, and reflexive separation) were examined. The bouncing regime, however, was not considered. A phenomenological model was established to predict both the onset of reflexive separation at  $B = 0$  and the complete boundary for  $B > 0$ .

Despite the substantial progress made to date on droplet collisions, several fundamental issues remain to be addressed. First, most existing studies employed assumptions or approximations with considerable uncertainties or limitations, due to the wide variation in length scales throughout the entire collision process. A unified framework based on direct numerical simulation is greatly desired to treat the multiscale physics of droplet collision with minimal uncertainties. The length scales and associated processes of concern range from macroscopic behaviors such as droplet deformation, the characteristic scale of which is on the order of the initial droplet diameter  $D$ , to microscopic behaviors such as gas-film drainage, for which the characteristic scale is down to an order of  $10^{-5}D$ . To this end, an efficient adaptive mesh refinement (AMR) technique<sup>25</sup> is required to render numerical calculations manageable without sacrificing the spatiotemporal resolution. Second, the first-principle prediction of the gas-film dynamics is needed, due to its importance in dictating the near-field interaction between droplets. Furthermore, a mechanistic understanding of both the head-on and the

off-center bouncing, as well as the associated gas-film evolution, is yet to be improved. A particular area of interest is the nonmonotonic coalescence–bouncing–coalescence transition with increasing Weber number. Third, the detailed flow and droplet evolution associated with separation outcomes must be explored. The experimental investigation of this phenomenon is formidable due to the underlying small-scale dynamics.

## II. NUMERICAL METHODS

### A. Conservation equations

The basis of the present study is the general numerical framework of the Gerris flow solver (<http://gfs.sf.net>). The formulation accommodates the conservation equations for an incompressible, variable-density flow with surface tension,<sup>30</sup> which is written in the following vector form:

$$\rho(\partial_t \mathbf{u} + \mathbf{u} \cdot \nabla \mathbf{u}) = -\nabla p + \nabla \cdot (2\mu \mathbf{D}) + \sigma \kappa \delta_s \mathbf{n}, \quad (5)$$

$$\nabla \cdot \mathbf{u} = 0, \quad (6)$$

where  $\mathbf{u} = (u, v, w)$  is the velocity vector,  $\rho(\mathbf{x}, t)$  is the fluid density,  $\mu(\mathbf{x}, t)$  is the dynamic viscosity, and  $\mathbf{D}$  is the deformation tensor, which is defined as  $D_{ij} = (\partial_i u_j + \partial_j u_i)/2$ . The Dirac delta function  $\delta_s$  expresses the fact that the surface tension,  $\sigma$ , is concentrated on the interface. The radius for the curvature of the interface is denoted by  $\kappa$ , and  $\mathbf{n}$  is the unit outward vector normal to the interface.

The VOF function  $c(\mathbf{x}, t)$  is introduced to trace the multifluid interface. It is defined as the volume fraction of a given fluid in each cell of the computational mesh. Thus, the density and viscosity can be expressed as follows:

$$\rho(c) \equiv c\rho_1 + (1-c)\rho_2, \quad (7)$$

$$\mu(c) \equiv c\mu_1 + (1-c)\mu_2, \quad (8)$$

where  $\rho_1, \rho_2$  and  $\mu_1, \mu_2$  are the densities and viscosities of the first and second fluids, respectively. According to the mass continuity, the advection equation for the density takes the following form in terms of volume fraction:

$$\partial_t c + \nabla \cdot (c\mathbf{u}) = 0. \quad (9)$$

A staggered temporal discretization of the volume fraction/density and pressure leads to a scheme that is second-order accurate in time.<sup>30</sup> A classical time-splitting projection method is used, which requires the solving of a Poisson equation. To improve the numerical efficiency and robustness, the discretized momentum equation is reorganized to a Helmholtz-type equation that can be solved using an improved multilevel Poisson solver. The resulting Crank–Nicolson discretization of the viscous terms is second-order accurate. Spatial discretization is achieved using graded octree partitioning in three dimensions. All the variables are collocated at the center of each discretized cubic volume. Consistent with the finite-volume formulation, the variables are interpreted as volume-averaged values for each cell. A piecewise-linear geometric VOF scheme generalized for quad/octree spatial discretization is used to solve the advection equation for the volume fraction.<sup>31</sup> The original

continuum surface force (CSF) approach<sup>31</sup> suffers from problematic parasitic currents,<sup>32</sup> and a combination of a balanced-force surface tension discretization and a height-function curvature estimation<sup>30</sup> is used to circumvent these problems. The Courant number is set to 0.8 for all the simulations to ensure overall numerical stability.

The mass transfer between droplets is quantified by introducing a dye variable, in light of the experimental study by Ashgriz and Poo.<sup>1</sup> The dye variable is numerically nondiffusive, so the mass transfer can be tracked during the droplet collision. The dye variable is restricted in the liquid phase and cannot enter the gas phase. Its initial value is set to be unity in one droplet and zero in the other. To visualize the spatiotemporal evolution of the dye variable, a photorealistic rendering of the numerical results is performed using the POV-Ray software tool (<http://www.povray.org/>). Surface and volume rendering are implemented for the liquid/gas surface and the dye media, respectively.

## B. Adaptive mesh refinement

This numerical method can resolve spatiotemporal variations in the flow field. The efficiency of a mesh adaptation can, thus, be substantially enhanced, particularly when addressing the reconnection and separation of interfaces.<sup>30</sup> Using local mesh refinement or coarsening in quad/octree discretization is also efficient, and it can be performed at every time step if necessary, with minimal impact on the overall performance. The interpolation of quantities on refined or coarsened cells is relatively simple on a regular Cartesian mesh, and it is performed conservatively for both momentum and the volume fraction.<sup>30</sup>

In the present paper, three refinement criteria are applied to regions of concern, namely, gradient-, phase-, and thickness-based criteria.<sup>25,33</sup> A faithful simulation of the droplet collision requires that the surface energy be adequately resolved. The gradient-based

refinement for the volume fraction ensures appropriate resolution along the interface. The kinetic energy in the liquid phase, which is comparable to the surface energy during the droplet collision, is also important. A fine mesh is required to avoid excessive numerical dissipation of kinetic energy. According to the value of the volume fraction for the liquid phase, the interior of the droplet is refined to an acceptable level. A thin gas film forms between the two droplets when they approach one another. The minimum thickness of the gas film may be several orders of magnitude smaller than the droplet diameter. It is computationally expensive to achieve this resolution by refining meshes in the entire interfacial region; it is also inconvenient if a manual adjustment of the mesh refinement is required during the simulation. To circumvent this difficulty, the thickness-based refinement method developed in our previous study<sup>25</sup> is implemented to ensure at least two grid cells within the thickness in resolving the thin gas film between interacting droplets. This approach significantly reduces the computational cost of capturing the lubrication phenomenon in the gas film. This method has been extensively validated<sup>25</sup> and applied to simulations of such complicated flow problems as impinging-jet atomization<sup>33</sup> and droplet interaction in a microfluidic channel under an electric field.<sup>34</sup>

## C. Computational setting

Two types of computational models are established. The first is a three-dimensional (3-D) model for off-center collision ( $B \neq 0$ ). Two spherical tetradecane droplets in a nitrogen environment are considered under atmospheric conditions. The initial distance between the two droplet centers is set to  $3D$ . The density ratio is 666, and the viscosity ratio is 119. Outflow conditions are imposed along the boundary of the computational domain ( $9D \times 9D \times 9D$ ). The second is an axisymmetric model simplified from the 3-D case

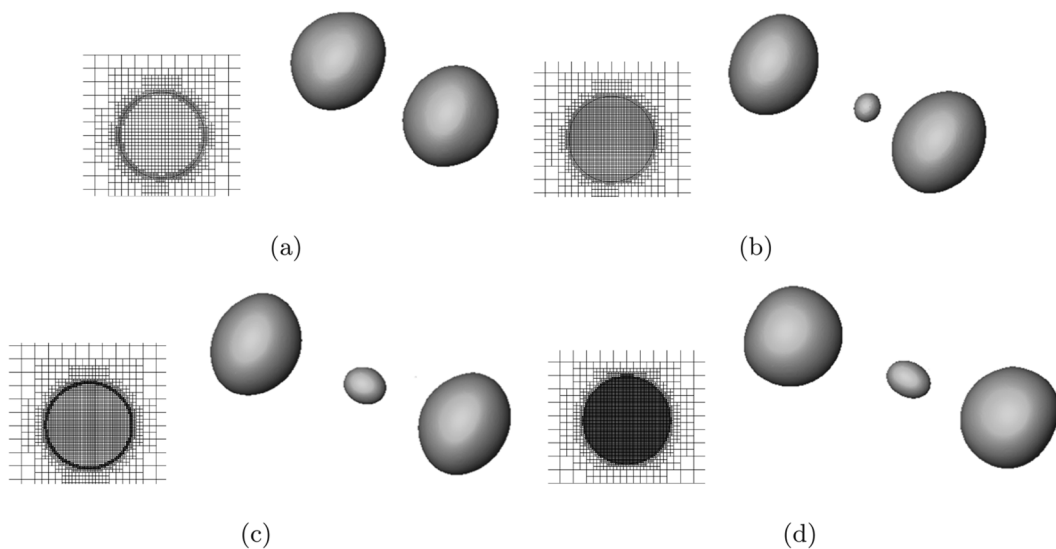


**FIG. 3.** Grid independence study (left: initial mesh for the droplet; right: instantaneous droplet configuration). The grid levels for the liquid phase and interface are: (a) 6 and 7, (b) 7 and 7, (c) 7 and 8, (d) 8 and 8, respectively.  $We = 61.4$ ,  $Re = 296.5$ ,  $B = 0.06$ , and  $D = 336 \mu\text{m}$ .

for head-on collision ( $B = 0$ ). The axisymmetric model assumes symmetry and considers only a quarter of the cross section of that of the 3-D model.

A grid independence study is for the 3-D model to ensure acceptable grid resolution for numerical accuracy. A near head-on collision resulting in reflexive separation with a satellite droplet for  $We = 61.4$ ,  $Re = 296.5$ ,  $D = 336 \mu\text{m}$ , and  $B = 0.06$  is selected from the experiment of Qian and Law<sup>4</sup> as a benchmark case. Two refinement criteria with different levels are tested, with phase-based refinement for the liquid phase and gradient-based refinement along the interface, with levels of  $L_p$  and  $L_g$ , respectively. The background mesh is fixed to level 4, with  $\sim 7$  mesh cells per initial droplet diameter. Maximum refinement level 8 is a mesh with  $\sim 112$  cells per initial droplet diameter. Four simulations with different combinations of  $L_p$  and  $L_g$  are performed. Figure 3 shows the initial meshes and droplet configurations at the same time for four different refinement levels. Figure 3(a) shows that no satellite droplet forms under  $L_p = 6$  and  $L_g = 7$ . Figure 3(b) shows that when  $L_p$  is increased to 7, the simulation can resolve the formation of the satellite droplet, likely because the numerical dissipation is lower inside the liquid phase than the case in Fig. 3(a). An additional increase in the  $L_g$  to 8 leads to the formation of a larger satellite droplet and a slightly larger distance between the two major droplets [see Fig. 3(c)]. Finally, when the  $L_p$  reaches 8, a slightly larger distance between the major droplets is observed, as shown in Fig. 3(d). Figure 4 compares the simulation result with  $L_p = 6$  and  $L_g = 7$  against the experimental images.<sup>4</sup> Since the results in Figs. 3(c) and 3(d) are almost identical, the combination of  $L_p = 7$  and  $L_g = 8$  is selected as a baseline to ensure the numerical accuracy. In most of the three-dimensional simulations, the number of numerical cells with AMR is  $\sim 600\,000$ , which amounts to  $\sim 50\,000\,000$  cells for a uniform mesh with the same interfacial resolution.

When two droplets approach one another, a stagnation point appears in the gas between the droplet surfaces. The resulting pressure buildup in the gas deforms the interfaces and retards the motion of the approaching surfaces, leading to the formation of a thin gas film. Based on the Reynolds equation that governs the pressure distribution in a thin film,<sup>35</sup> the pressure reaches its maximum at the center and minimum at the gas-film boundary. Hence, the thickness of the gas film varies spatially along the radial direction. The thickness of the gas film also varies due to the motion and deformation of the droplets. To understand the dynamics of the gas film and its role in determining the collision outcome, thickness-based criteria<sup>25</sup> are applied to the basic refinement setting. Because the axisymmetric model includes only a quarter of the cross section of the 3-D model, a distance-oriented, thickness-based criterion<sup>25</sup> is imposed on the collision plane, which is the axis of symmetry between the two droplets. This approach allows us to use a grid resolution that is high enough to avoid unphysical merging caused by the insufficient grid resolution for the bouncing outcome.

Figure 5 shows the detailed grid at different magnification levels at the moment of maximum deformation during a typical head-on collision. A minimum of three grids are applied to the gas film to simulate the flow dynamics accurately. The refinement level increases automatically with a film thickness up to level 15 with a grid size of  $\sim O(10^{-5})$  times the undeformed droplet diameter. Simulations with such a high resolution provide good insight

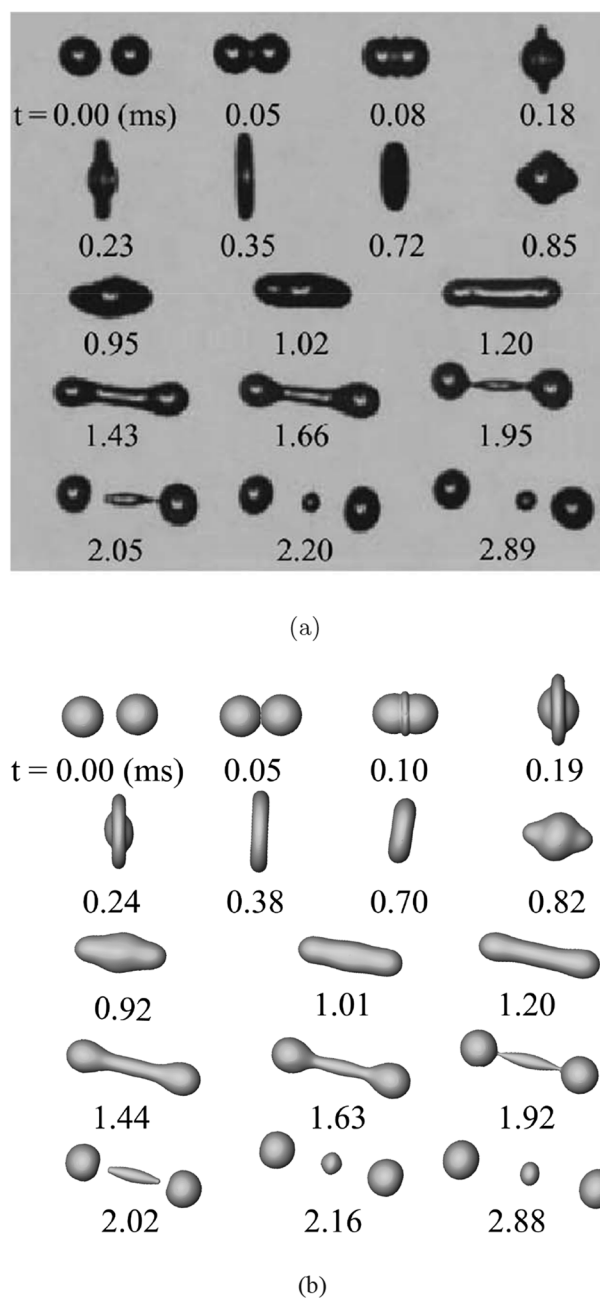


**FIG. 4.** Temporal evolution of separation collision: (a) experimental images from Ref. 4 (Reproduced with permission from J. Qian and C. K. Law, "Regimes of coalescence and separation in droplet collision," *J. Fluid Mech.* **331**, 59 (1997). Copyright 1998 Cambridge University Press); (b) present simulation results. Tetradecane droplets in nitrogen,  $We = 61.4$ ,  $Re = 296.5$ ,  $B = 0.06$ ,  $D = 336 \mu\text{m}$ , and  $U = 2.48 \text{ m/s}$ , at 1 atm.

into the underlying physics of the gas-film dynamics. Off-center bouncing is also considered; a topology-oriented, thickness-based criterion<sup>25</sup> is implemented in the 3-D model. Unlike the distance-oriented criterion, the topology-oriented criterion can resolve any

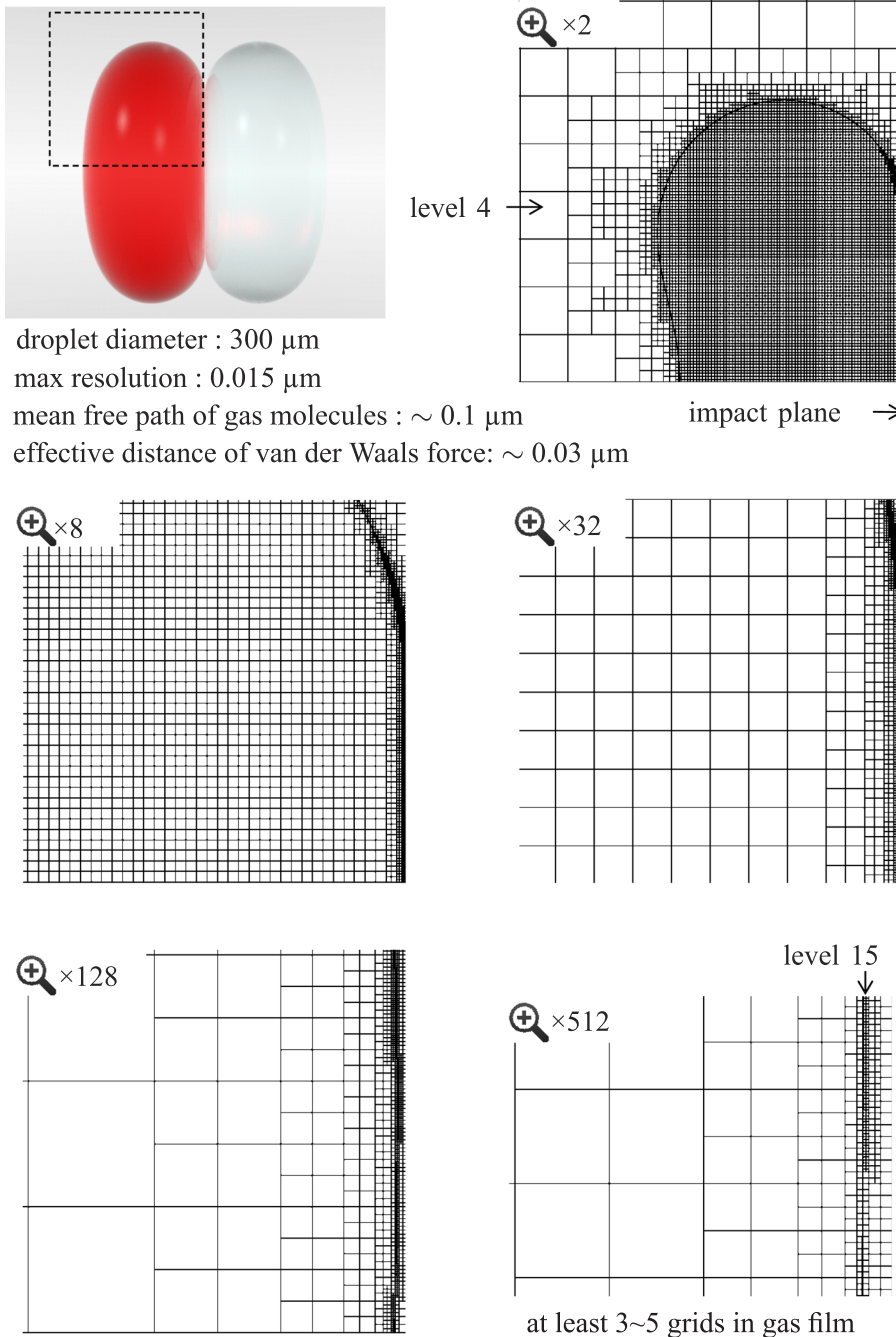


FIG. 5. Detail of numerical grid used in simulation of bouncing droplets.

30 August 2024 21:57:05

thin region under arbitrary conditions. This capability makes the topology-oriented criterion ideal for addressing off-center bouncing involving complicated shape variations and gas-film motions.

In the present paper, the Weber number  $We$  and impact factor  $B$  cover ranges of 0–125 and 0–1, respectively, as shown in the regime diagram in Fig. 2. Both surface rendering for the

liquid/gas surface and volume rendering for dye media are used to provide photorealistic images of the shape evolution of the merged droplets. Thus, the spatial evolution of the collided mass from each of the droplets is visualized. Realistic data visualization will help us to reveal the detailed dynamics of the flow evolution and mass transfer.

### III. RESULTS AND DISCUSSION

#### A. Bouncing

As mentioned in the Introduction, it remains challenging to introduce the molecular force into the continuum fluid dynamics framework accurately. To focus on the effects of flow dynamics inside the gas film during the transitions from the merging to the bouncing mode, the molecular force is not considered here. Hence, the distance for merging is determined by the minimum grid size. This grid size can be estimated using experiments. In the present paper, the interface around the thin gas film is extensively refined to resolve the flow field inside the film with the implementation of the distance-oriented refinement criterion.<sup>25</sup> If necessary, the minimum grid size can be minimized to less than the effective distance of the van der Waals force, to numerically disable merging. In this way, the effect of gas-film lubrication on the bouncing dynamics can be investigated symmetrically over a wide range of  $We$  values.

#### 1. Head-on bouncing (region II, $B = 0$ )

Figure 6 shows rendered images of the head-on bouncing of tetradecane droplets in nitrogen under  $p = 1$  atm and  $We = 8.6$ . A

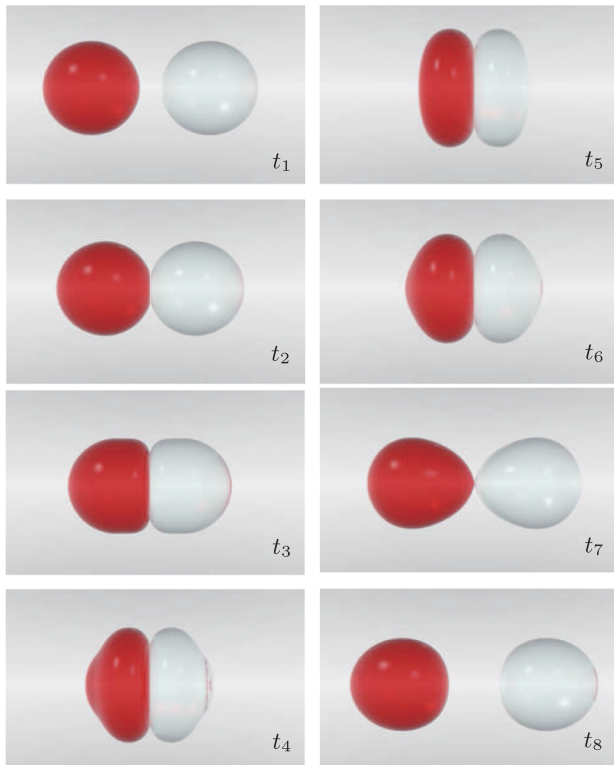


**FIG. 6.** Head-on bouncing. Tetradecane droplets in nitrogen at 1 atm.  $We = 8.6$ ,  $Re = 105.9$ ,  $B = 0$ ,  $D = 306 \mu\text{m}$ ,  $U = 0.97$  m/s. Reproduced with permission from X. Chen and V. Yang, "Thickness-based adaptive mesh refinement methods for multi-phase flow simulations with thin regions," *J. Comput. Phys.* **269**, 22 (2014). Copyright 2014 Elsevier, Inc.

flat gas film forms at  $t_2$  to prevent the merging of the approaching droplets. The diameter of the gas film continues to increase through  $t_5$ , while the liquid inertia flattens the spherical droplet. Since droplets with spherical shapes have minimum surface energy, the deformed droplets begin to recover their spherical shapes after achieving maximum deformation at  $t_5$ . The droplets indirectly interact through the pressure accumulation in the gas film, which produces motions opposite to the initial motions of the droplets, thereby separating the droplets from each other to complete the bouncing process.

Figure 7 shows the shape evolution of the gas film at  $We = 1.0$ . The coordinate system is stretched in the collision direction to enhance visualization. When the droplets approach one another as shown in Fig. 7(a), the surface flattens and a dimple pattern begins to form [Fig. 7(b)]. The thickness of the gas film decreases when the droplet continues to flatten. As the droplets continue their approach, the gas drainage process diminishes, with a slow variation in the dimple curvature of the film thickness, as shown in Figs. 7(d)–7(f). Following maximum deformation, a reverse process takes place, and the droplets start to recover their original configuration, as shown in Figs. 7(g)–7(i).

The time required for bouncing can be measured from the evolution of the droplet interfaces. This method, however, more or less arbitrarily determines the moments of the beginning and termination of the interaction. For consistency, bouncing time  $\tau_b$  is defined here by the period when the pressure in the center of the gas film is higher than the ambient pressure. Figure 8(a) shows the relationship between the droplet bouncing time  $\tau_b$  as normalized by the convective time  $\tau_c = D/U_r$  and the square root of the Weber number. A simple correlation is obtained as follows:

$$\tau_b/\tau_c = 0.82\sqrt{We} \quad (0.2 < We < 8.6). \quad (10)$$

The above expression can be rearranged as follows:

$$\tau_b = 0.82\sqrt{\rho D^3/\sigma}. \quad (11)$$

It is interesting to note that the bouncing time is close to the natural oscillation time of a spherical droplet as follows:<sup>36</sup>

$$\tau_o = \frac{\pi}{4}\sqrt{\rho D^3/\sigma} \approx 0.79\sqrt{\rho D^3/\sigma}. \quad (12)$$

The same observation was made by Nobari *et al.*<sup>17</sup> During  $\tau_b$ , the two droplets oscillate near the collision plane. Droplet bouncing is, thus, analogous to the oscillation of a droplet in partial contact with a solid surface. Yamakita *et al.*<sup>37</sup> showed that the oscillation period decreased with the increasing contact area. In reality, bouncing is caused by the formation of the gas film and the pressure buildup between the approaching droplets. The gas film varies in shape during bouncing; it is difficult to establish a theoretical model for the equivalent contact area. Since the average contact area increases as the Weber number increases, the bouncing time should decrease accordingly. Figure 8(b) shows the relationship between the droplet bouncing and the vibration time as a function of  $We$ . A correlation is obtained as follows:

$$\tau_b/\tau_o = 0.29We^{-0.35} + 0.88. \quad (13)$$

The two time scales become asymptotically equal for a large Weber number.

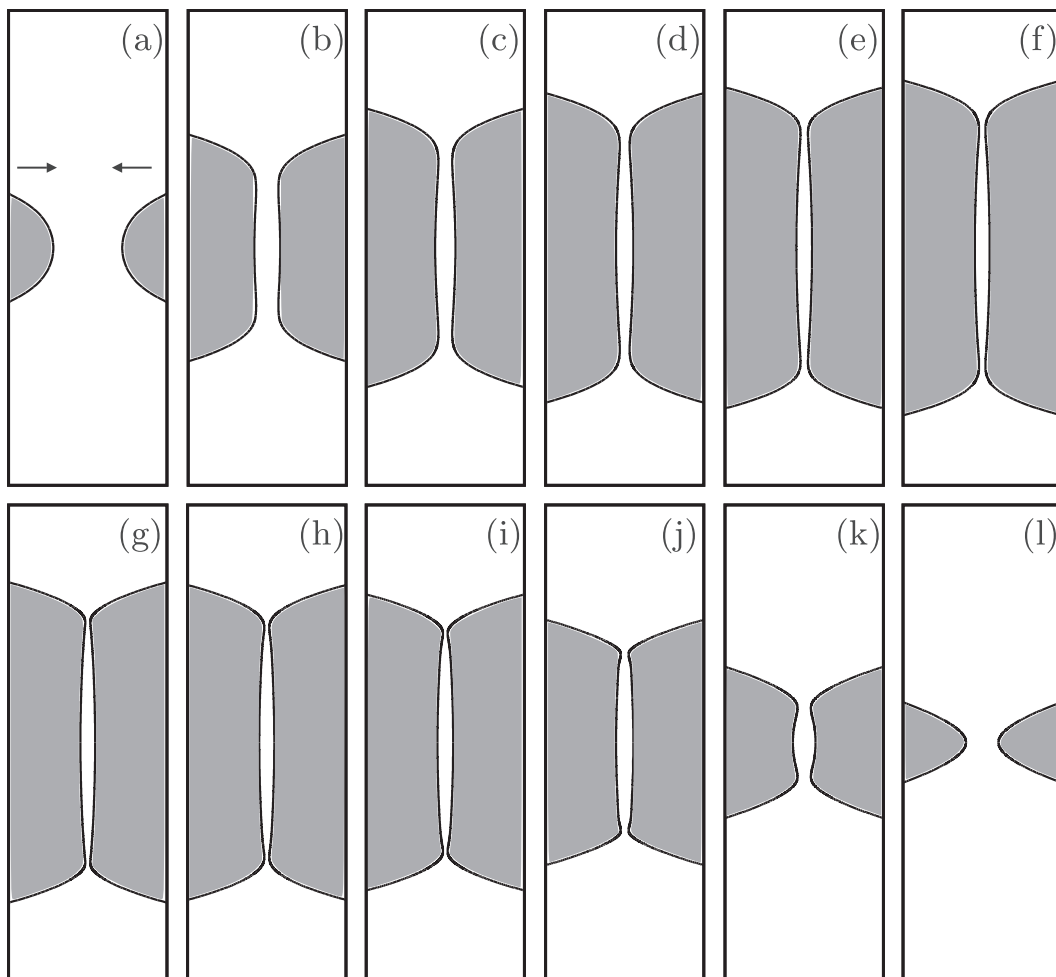
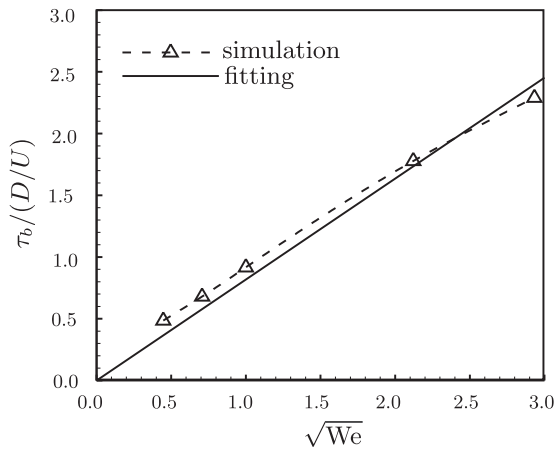


**FIG. 7.** Evolution of gas film during head-on bouncing. Tetradecane droplets in nitrogen at 1 atm.  $We = 1$ ,  $Re = 36.1$ ,  $B = 0$ ,  $D = 306 \mu\text{m}$ ,  $U = 0.33 \text{ m/s}$ . The coordinate system in the collision direction is elongated uniformly to enhance visualization.

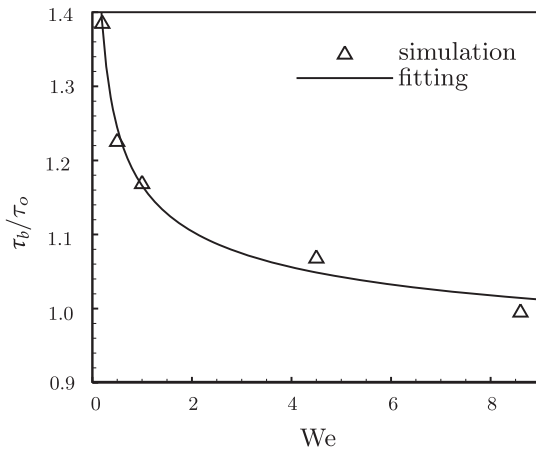
## 2. Off-center bouncing (region II, $B \neq 0$ )

For an off-center collision with  $B \neq 0$ , the interaction of the two droplets involves not only the motion across their centers but also a sliding motion. Figure 9 shows the situation when two equal-sized droplets are brought into contact, with the relative velocity parallel to the horizontal plane. The dashed line represents the impact plane, which is the common tangent plane at the contact point of the two spherical droplets. To facilitate analysis, the two droplets are rotated so that the impact plane is parallel to the horizontal axis (Fig. 9, right). The droplet velocity can be decomposed into two components,  $U_n$  and  $U_p$ , which are normal and parallel to the impact plane, respectively. The normal motion accounts for the interaction of the droplets at the impact plane, whereas the parallel motion keeps the droplets moving apart. This configuration will be used in the rest of this paper to provide a convenient framework to study the collision dynamics.

A 3-D simulation for off-center bouncing is performed for  $We = 48.8$  and  $B = 0.9$ . The topology-oriented AMR<sup>25</sup> is employed to substantially reduce the computational cost. The resolution of the gas film is improved to a resolution with a minimum grid size of  $\sim 0.7 \mu\text{m}$ ,  $\sim O(10^{-3})$  times the droplet diameter. Note that the gas film was usually left out in previous numerical studies of off-center bouncing.<sup>38–40</sup> For example, the approach of two VOF functions was adopted to track the interface of each liquid droplet separately to always prompt droplet bouncing.<sup>38</sup> Figure 10 shows the evolution of the collision dynamics with photorealistic rendering. At  $t_1$ , two droplets are brought together with a small gap between them. A gas film forms in the interaction region where flow stagnation occurs. Positive pressure is established within the gas film and prevents droplet merging. The two droplets eventually bounce apart without ever coming into direct contact. The parallel component of collision motion is a translation squeezing action that results from the translation of inclined surfaces caused by normal



(a)



(b)

**FIG. 8.** (a) Bouncing time normalized by droplet convective time  $D/U$ ; (b) bouncing time  $\tau_B$  normalized by natural oscillation time  $\tau_o$ .

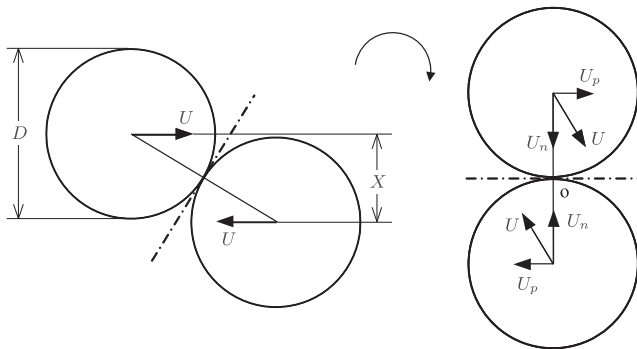


**FIG. 9.** Classical and transformed views of binary droplets at collision.

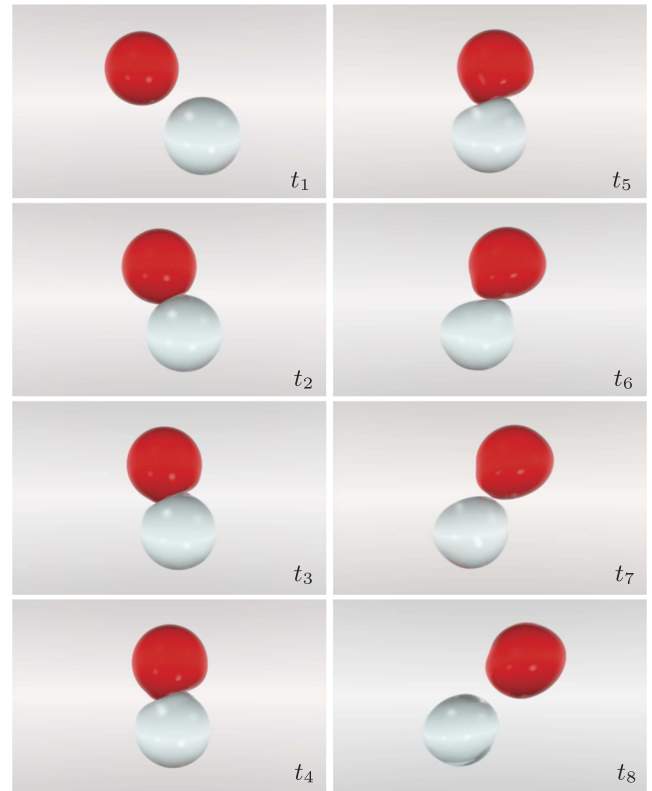


**FIG. 10.** Time evolution of off-center bouncing. Tetradecane droplets in nitrogen at 1 atm.  $We = 48.8$ ,  $Re = 260.3$ ,  $B = 0.9$ ,  $D = 306 \mu\text{m}$ ,  $U = 2.31 \text{ m/s}$ . Reproduced with permission from X. Chen and V. Yang, "Thickness-based adaptive mesh refinement methods for multi-phase flow simulations with thin regions," *J. Comput. Phys.* **269**, 22 (2014). Copyright 2014 Elsevier, Inc.

motion. The local film may be squeezed by the sliding of the inclined surface.

Figure 11 shows the detailed shape evolution of the gas film. It rotates with respect to the collision center. The length of the gas film increases from  $t_1$  to  $t_4$  under the impact motion normal to the contact surface and then decreases from  $t_4$  to  $t_9$  due to the slip motion tangential to the contact surface. The thickness of the gas film decreases from  $t_1$  to  $t_6$ , during which time the impact motion continues to squeeze the gas out of the interaction zone. The droplets move apart before the rupture of the gas film. Figure 12 shows the velocity and pressure distributions in the gas film at  $t_4$ . A low-velocity field is observed, and the pressure field is nearly uniform. The enlarged image near the collision center shows that the two droplet surfaces move in parallel to the gas film, indicating a lubrication effect.

### 3. Gas-film evolution

To understand the shape evolution of the gas film, the simulation results for head-on bouncing are investigated in detail. When two droplets approach each other, pressure builds up near the stagnation (collision) point. The droplets then deform and form a

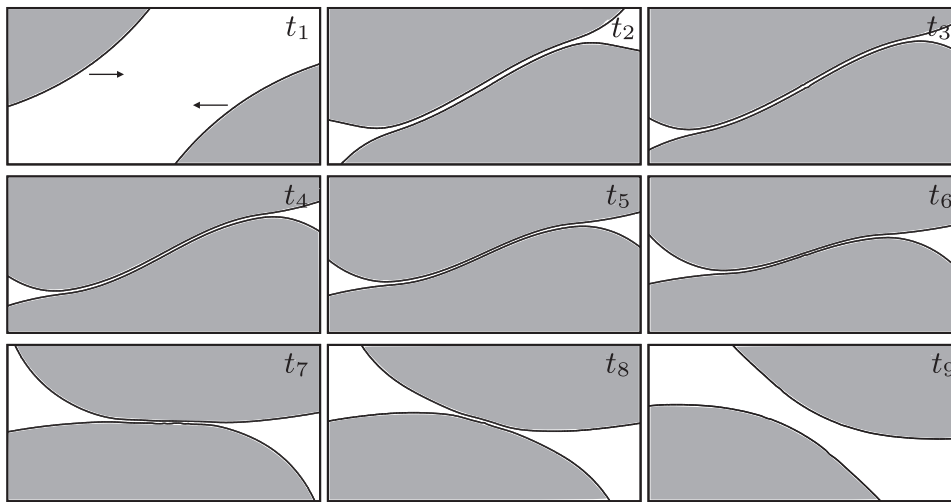


FIG. 11. Detailed shape evolution of gas film during off-center bouncing.

dimple; the high-pressure gas film that forms between the droplets prevents them from merging. The maximum film thickness,  $h_{center}$ , is located on the collision axis, and the minimum film thickness  $h_{min}$  is at the rim of the dimple with a radius of  $r_h$ , as shown schematically in Fig. 13. Figure 14 shows the evolution of the droplet surface near the impact plane for  $We = 1.0$ . The time interval between consecutive droplet surface contours is constant. The upper half of the figure shows the droplet approach, and the lower half shows the bouncing off situation.

Figure 15(a) shows the evolution of the gas-film thicknesses  $h_{min}$  and  $h_{center}$  and rim radius  $r_h$ . All the quantities are normalized by the initial droplet diameter and velocity  $U$ . Considering Figs. 15(a) and 7 together, the gas-film topology can be understood

in detail. When the two droplets approach each other, the interface flattens and a dimple pattern with a radius of  $r_h$  begins to form. A positive pressure field is established in the gas film. Initially,  $h_{min}$  and  $h_{center}$  are equal because of the spherical shape of the droplets, as shown in Fig. 15(a). Once the gas film forms, the decreases in  $h_{min}$  and  $h_{center}$  are resisted by the gas-film lubrication. The change in  $h_{center}$  is slower than that in  $h_{min}$  due to the occurrence of stagnation at the collision center. When the inertia of the droplet cannot further drain the gas film, the droplet starts to recover its original shape under the effect of the surface tension. The overall gas-film thickness begins to increase as the droplets move apart.  $r$  decreases under the recovery motion, along with a slightly increasing  $h_{center}$ . This increase is primarily attributed to the shrinkage of the dimple

30 August 2024 21:57:05

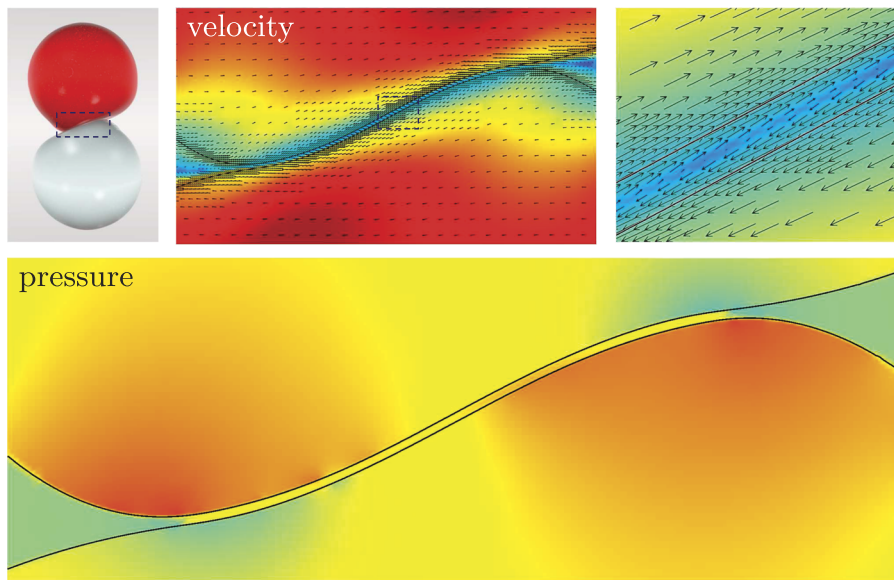
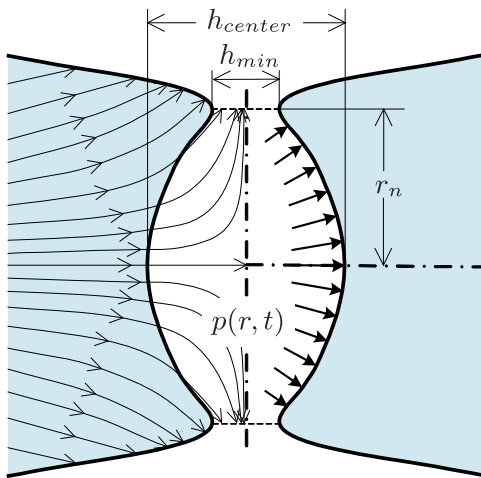


FIG. 12. Pressure and velocity distribution near the gas film during off-center bouncing.



**FIG. 13.** Schematic diagram of droplet configuration and streamlines near the impact plane at  $We = 1$ .

shape, which pushes the mass in the gas film near the rim radially toward the collision center. However,  $h_{min}$  continues to decrease for a while and then shows a rapid increase (a further decrease in  $h_{min}$  may induce coalescence). Before the droplets bounce apart, a sudden decrease is observed for both  $h_{min}$  and  $h_{center}$ , while  $r$  reaches zero quickly. Afterward,  $h_{min}$  and  $h_{center}$  coincide, indicating the disappearance of the dimple shape and the bouncing of the droplets.

The gauge pressure on the impact point  $(0, 0)$  is registered to help us understand the local shape evolution, as shown in Fig. 15(b). A positive pressure field begins to be established in the gas film, as shown at  $t_1$ , indicating the formation of a dimple gas film. The overall pressure increases through  $t_2$  and  $t_3$ . The maximum pressure is reached in the collision center at  $t_3$ . Afterward, a more uniform distribution along the impact plane is achieved across the dimple radius

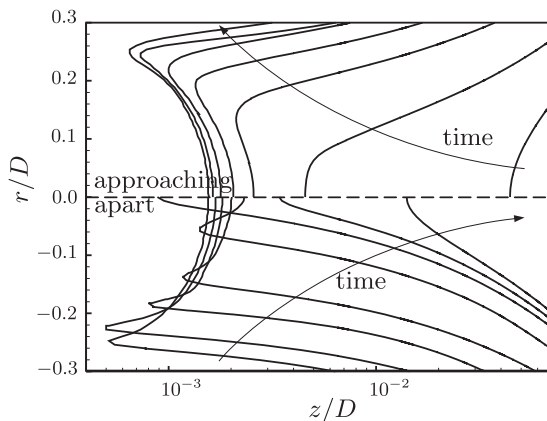
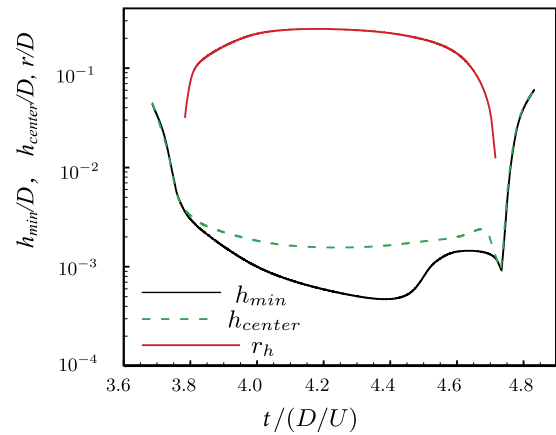
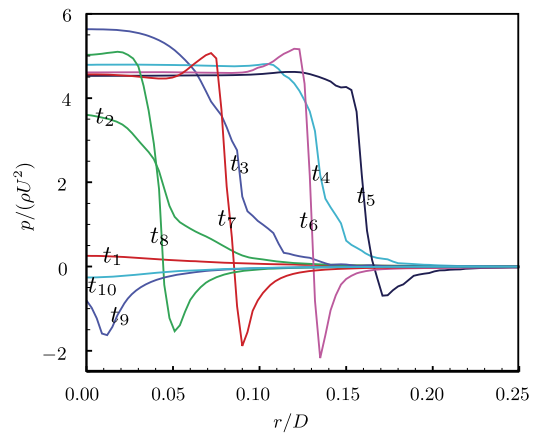


**FIG. 14.** Evolution of droplet surface interface evolution. Tetradecane droplet in nitrogen at  $p = 1$  atm and at  $We = 1$ .



(a)



(b)

**FIG. 15.** (a) Evolution of geometric parameters of gas film,  $h_{min}$ ,  $h_{center}$ , and  $r$ , tetradecane droplet in nitrogen at  $p = 1$  atm and  $We = 1$ ; (b) pressure profiles at the collision plane at  $We = 1$ .

at  $t_4$ . The maximum deformation is achieved at a moment between  $t_4$  and  $t_5$ . At  $t_5$ , the recovered motion of the interface introduces a radial flow motion toward the interior of the gas film to cause a negative gauge pressure near the rim of the gas film. It causes a further decrease in  $h_{min}$  at the commencement of the bouncing off [see Fig. 15(a)]. Moreover, the radial shrinking motion of the dimple induces compression in the gas film. A pressure peak inside the gas film is observed near the rim at  $t_6$  and  $t_7$ . Thus, a sharper rim occurs during bouncing off than during the approach of the droplets. The negative pressure region moves to the collision center at  $t_9$ . The dimple shape changes and quickly becomes spherical, which causes sudden decreases in  $h_{min}$  and  $h_{center}$ . Then, the pressure distribution relaxes to the ambient value at  $t_{10}$ .

Previous experiments<sup>7</sup> showed that for the head-on collision of tetradecane droplets in nitrogen at 1 atm, the collision outcome changes from merging to bouncing as  $We$  increases to 1.88 and from

bouncing to merging as  $We$  further increases to 10.3. To understand this nonmonotonic variation in the merging and bouncing, five head-on collisions at  $We = 0.2, 0.5, 1.0, 4.5,$  and  $8.6$  are simulated using the topology-oriented AMR. Special attention is given to the spatial resolution of the gas-film dynamics since this information is difficult to estimate from experiments.<sup>7</sup> The interfacial region near the gas film is refined to a grid size of  $\sim 0.015 \mu\text{m}$ , which is much lower than the effective distance of the van der Waals forces. Merging outcomes are, thus, avoided numerically for  $We = 0.2, 0.5,$  and  $1.0$ . In this way, the collision dynamics at the five different  $We$  numbers can be systematically considered through comparisons.

The nonmonotonic variation in bouncing and coalescence during the head-on collision ( $B = 0$ ) with the increasing Weber number was observed by Qian and Law.<sup>4</sup> The full understanding of this behavior requires systematic investigation into the gas-film dynamics as a function of Weber number. Figure 16 shows the time evolution of the pressure at the collision center over  $We = 0.2$ –61.4. The pressure reaches its peak value when the dimple is about to form between the droplet surfaces. Afterward, the pressure decreases quickly with the deformation of the approaching surfaces. For bouncing cases, constant pressure is observed for the existing gas films. When normalized by  $\rho U_r^2$ , the constant pressures for different Weber numbers collapse, suggesting that the pressure buildup in the gas film is a function of Weber number. The resistance of the gas film increases with the increasing Weber number.

Figure 17 shows the gas-film shapes at the occurrence of maximum deformation for various Weber numbers. The dimple radius increases with the increasing Weber number. Different behaviors in the minimum thickness are observed for  $We < 1$  and  $We > 1$ . When  $We < 1$ , the minimum film thickness increases as the Weber number increases. The minimum film thickness decreases with the increasing Weber number for  $We > 1$ . When  $We < 1$ , the surface tension resists the droplet deformation caused by liquid inertia. The increase in the difference between the maximum and minimum film thicknesses is slower than the increase in the average film thickness. Thus, the rim of the gas film moves away from the impact plane and subsequently increases in the minimum film thickness. When

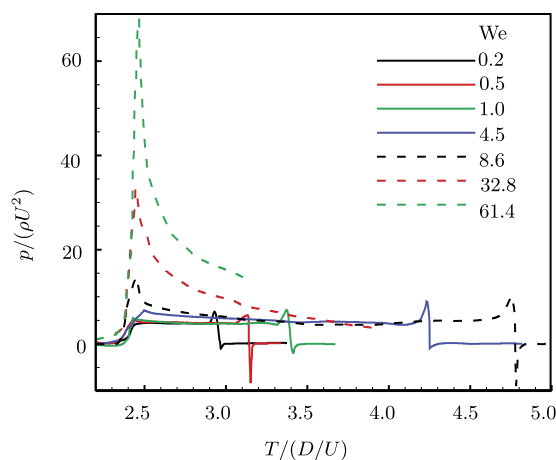


FIG. 16. Evolution of pressure at the collision center with different Weber numbers.

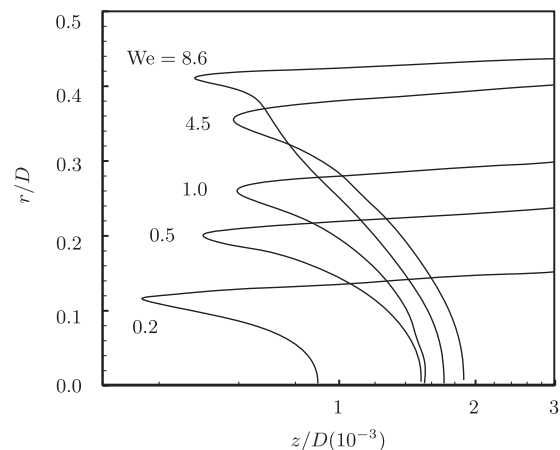


FIG. 17. Gas film shapes at occurrence of maximum deformations for five Weber numbers.

$We > 1$ , the droplet inertia dominates the flow evolution, ensuing droplet deformation. Although the gas film is harder to squeeze out, the inertia of the droplets can still enlarge the dimple size and decrease the minimum film thickness. Overall, the minimum film thickness shows a nonmonotonic behavior with the increasing Weber number. The associated collision outcomes exhibit the same trend.

## B. Coalescence and separation

Over forty 3-D simulations are performed under various Weber numbers (30–120) and impact factors (0–0.75) to explore the droplet interactions after droplet merging. The three different types of collision outcomes shown in Fig. 2, coalescence after substantial deformation, reflexive separation, and stretching separation, are studied in detail. The results show good consistency with the regime diagram obtained experimentally by Qian and Law.<sup>4</sup>

### 1. Coalescence (regime III)

Figure 18 shows the evolution of the gas film between the droplets for head-on coalescence at  $We = 32.8$ . At  $t_1$ , a gas film forms at the center to prevent droplet merging. Because the droplets cannot cross the collision plane, the liquid mass accumulates toward the gas film. The interfaces start to ripple near the rim of the gas film. From  $t_2$  to  $t_7$ , both  $h_{\text{center}}$  and  $h_{\text{min}}$  decrease, whereas  $r_n$  increases. The maximum value of  $r_n$  occurs at approximately  $t_7$ . As  $h_{\text{min}}$  reaches the minimum grid size at  $t_8$ , the interfaces merge and rupture the gas film at the rim. The gas film is then isolated from the ambient environment. Surface tension then drives the rim toward the center of the gas film (see snapshots at  $t_8$  and  $t_9$ ). In addition, the interfaces outside the gas film merge and expand in the radial direction. The size of the rim increases between  $t_9$  and  $t_{11}$  due to the accumulation of the trapped gas phase. The shrinkage motion forms an elliptical gas bubble at  $t_{12}$ . The gas bubble eventually becomes spherical under the effect of the surface tension. It is noted that the rupture of the gas film may not be completely axisymmetric due to the flow instability.

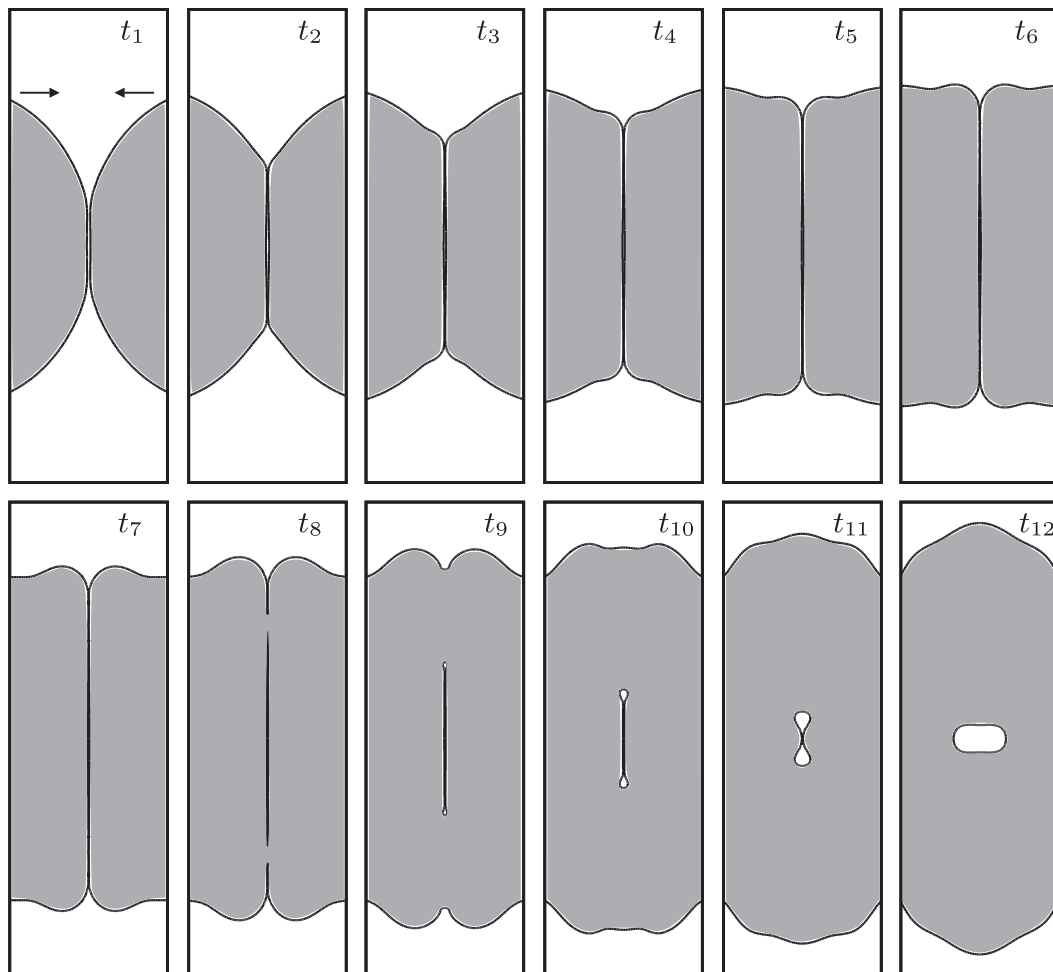


**FIG. 18.** Evolution of gas film rupture under head-on collision. Tetradecane droplets in nitrogen at 1 atm.  $We = 32.8$ ,  $Re = 206.8$ ,  $B = 0$ ,  $D = 306 \mu\text{m}$ ,  $U = 1.89 \text{ m/s}$ .

Figure 19 shows a time sequence of rendered images for an off-center collision resulting in coalescence with  $B = 0.2$  and  $We = 60$ . After merging at  $t_2$ , the combined mass is pushed outward laterally to form a liquid rim that spreads at the impact plane. A small bubble is observed, resulting from the rupture of the gas film between the droplets. The rim reaches its maximum size at  $t_3$ . The rim shape then shrinks under the surface tension force. Since the cross section of the rim has an elliptical shape on the impact plane, the minor axis recovers earlier than the major axis in the direction of the  $U_p$ . The shrinkage of the liquid rim in the direction of the minor axis forms a flat shape at  $t_4$ . Since parallel motion keeps its original direction in an off-center collision, rotation occurs around the collision center in the following sequence. The recovery of the major axis of the liquid rim begins to squeeze the mass to the collision center at  $t_5$ . The mass is pushed back to its original location. A ligament with a maximum length in the direction of  $U_n$  is obtained at  $t_6$ . Subsequently, the ligament is shortened under the surface tension effect, as shown from  $t_7$  to  $t_8$ . One single spherical droplet with

a mass equal to that of the two original droplets eventually forms. The bubble inside the combined droplet is located near the impact center.

## 2. Separations (regime IV and V)

Figure 20 shows a time sequence of rendered images for an off-center collision resulting in reflexive separation with  $B = 0.06$  and  $We = 61.4$ . A major difference from the coalescence case shown in Fig. 19 is the shrinkage of the liquid rim, which causes a strong reflexive motion and the elongation of the combined droplet. The ligament becomes long enough that the end-pinching mechanism<sup>41</sup> caused by the round ends causes it to break apart. A satellite droplet forms between two large droplets. Figure 21 shows the evolution of an off-center collision resulting in stretching separation, with  $B = 0.49$  and  $We = 65.1$ . The oscillation of the liquid ligament is similar to the coalescence case in Fig. 19. However, the  $U_p$  strongly elongates the combined droplets in the parallel direction, eventually

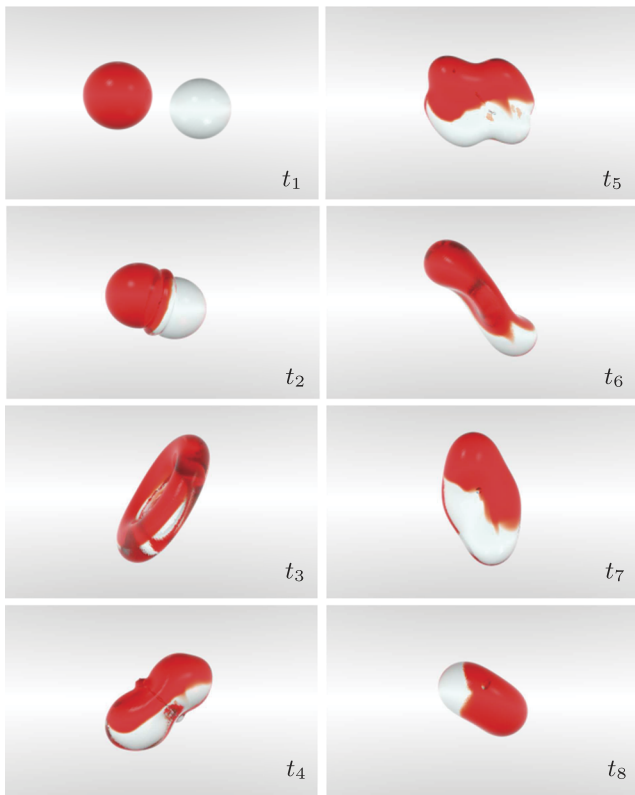


FIG. 19. Off-center coalescence. Tetradecane droplets in nitrogen at 1 atm,  $We = 60$ ,  $Re = 283.1$ ,  $B = 0.2$ ,  $D = 336 \mu\text{m}$ ,  $U = 2.37 \text{ m/s}$ .

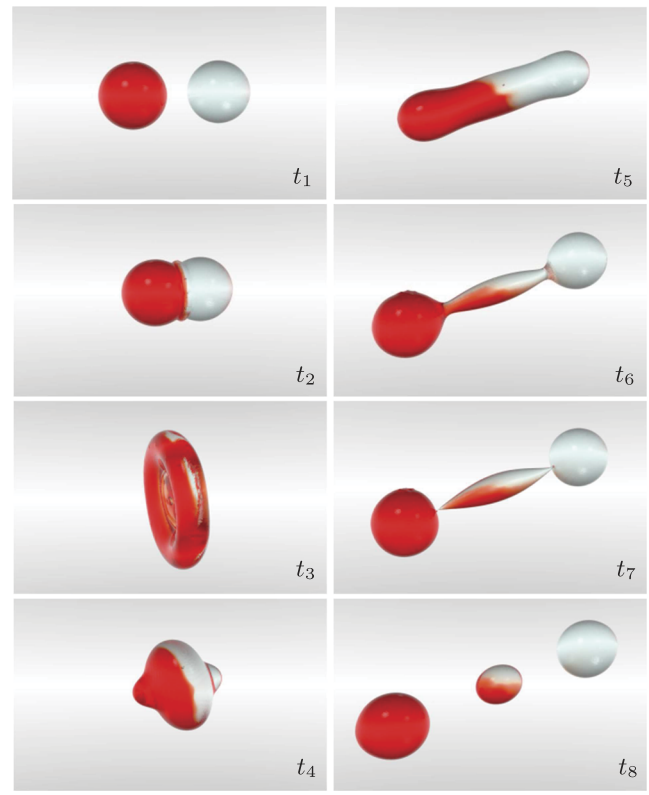


FIG. 20. Reflexive separation. Tetradecane droplets in nitrogen at 1 atm,  $We = 61.4$ ,  $Re = 296.5$ ,  $B = 0.06$ ,  $D = 336 \mu\text{m}$ ,  $U = 2.48 \text{ m/s}$ .

causing droplet breakup. Multiple satellite droplets form between the two large droplets. The sizes of the satellite droplets are usually smaller than those in the reflexive separation case.

To further understand the underlying mechanism of the collision dynamics, the energy budgets for the two separation outcomes are analyzed, along with a consideration of the shape and flow evolution. The total energy (TE) of the system consists of kinetic energy (KE), surface energy (SE), and cumulative viscous dissipation energy (DE).<sup>18</sup> The KE is calculated using a volume-weighted sum of kinetic energy over the liquid phase. The product of the surface tension and surface area gives the SE. The DE is calculated by taking the time integral of a volume-weighted sum of the viscous dissipation rate (VDR) over the liquid phase. The VDR is given by a dissipation function<sup>42</sup> as shown below:

$$\Phi = \mu \left[ 2 \left( \frac{\delta u}{\delta x} \right)^2 + 2 \left( \frac{\delta v}{\delta y} \right)^2 + 2 \left( \frac{\delta w}{\delta z} \right)^2 + \left( \frac{\delta v}{\delta x} + \frac{\delta u}{\delta y} \right)^2 + \left( \frac{\delta w}{\delta y} + \frac{\delta v}{\delta z} \right)^2 + \left( \frac{\delta u}{\delta z} + \frac{\delta w}{\delta x} \right)^2 \right] + \lambda \left( \frac{\delta u}{\delta x} + \frac{\delta v}{\delta y} + \frac{\delta w}{\delta z} \right)^2, \quad (14)$$

where  $\mu$  is the liquid viscosity,  $(u, v, w)$  and  $(x, y, z)$  are velocity components and spatial coordinates, respectively, and  $\lambda$  can be expressed as  $-2/3\mu$  according to Stokes' hypothesis.

Figure 22 shows the energy budget for (a) reflexive separation and (b) stretching separation. The TE of the system is well conserved. Figure 23 shows the interfaces and velocity vectors on the cross section corresponding to the energy budget for reflexive separation [see Fig. 22(a)]. Before deformation, the surface and kinetic energies are constant. At  $t = 0.4$ , the droplets start to deform and a gas film forms between the droplets. The spherical surface is flattened around the collision center; both SE and KE decrease slightly. At  $t = 0.5$ , the VDR and DE increase rapidly as soon as the interfaces merge. As the two droplets move closer, KE, SE, and VDR decrease, while DE continues to increase. SE reaches a minimum at  $t = 0.6$ , the instant when the gas film breaks into spherical bubbles. Afterward, KE is transformed to SE under the effect of droplet inertia. SE reaches a maximum at  $t = 1.6$ , while KE continues to decrease until the gas film reaches its thinnest at  $t = 1.7$ . When the surface tension in the bounding rim withdraws the mass to the impact center, the SE is transferred to KE and DE. Note that the velocity of the thin liquid film is zero. Another peak of viscous dissipation appears when the mass around the film joins at the collision center. The deformation of the rim causes inverse motions in the colliding mass of the droplets. The second trough of SE takes place at  $t = 2.5$  during the recovery from the deformation. The KE reaches its second crest at  $t = 2.6$ . The inverse motion elongates the combined droplet. Moreover, the KE continues to transfer to SE and DE. A second minimum

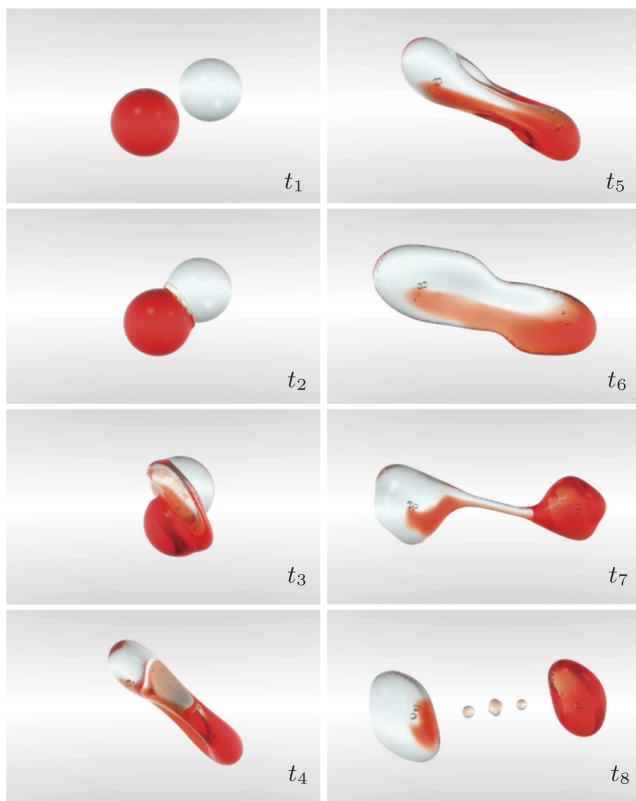


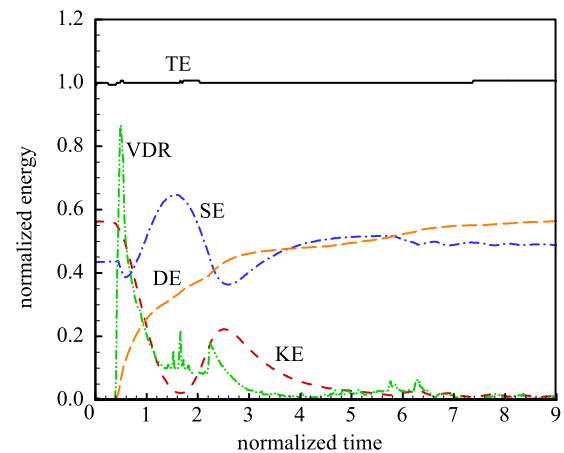
**FIG. 21.** Stretching separation. Tetradecane droplets in nitrogen at 1 atm,  $We = 65.1$ ,  $Re = 320.3$ ,  $B = 0.49$ ,  $D = 370 \mu\text{m}$ ,  $U = 2.43 \text{ m/s}$ .

KE is observed at approximately  $t = 5.8$  when the ligament breaks near the round ends.

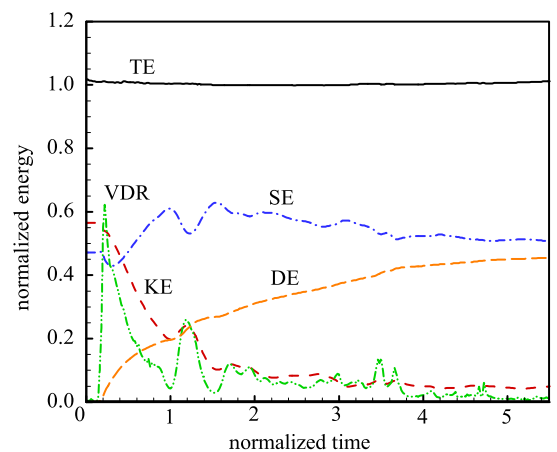
Figure 24 shows the evolution of the interface and velocity vectors on the cross section for stretching separation. The corresponding energy budget is given in Fig. 22(b). The energy variation and flow development from the beginning of the deformation to the first minimum SE are similar to their counterpart in reflexive separation. The droplet begins to deform at  $t = 0.1$ . The VDR shows a peak at  $t = 0.2$ . SE reaches a maximum at  $t = 0.3$ . The first trough of KE is also observed at  $t = 1.0$  when a thin gas film forms in the impact plane. After reaching a crest value, the SE decreases due to the combined effects of the reflexive motion resulting from the evolution of the rim. The first crest of the KE is observed at  $t = 1.2$ . When all the KE from the reflexive motion is transferred again to SE and DE, the KE reaches a second trough with a flat shape at  $t = 1.5$ . Afterward, the liquid ligament oscillates near the collision center. The stretching motion continues to elongate the liquid ligament, transferring the KE of the noninteracting mass to SE. The thin liquid ligament eventually breaks into two large droplets and a number of small satellite droplets.

### 3. Interacting volume and surface

The existing models in the classic approach treat the interacting region as an overlapping region, as in Ashgriz and Poo.<sup>1</sup> Based



(a)



(b)

**FIG. 22.** Energy budget for (a) reflexive separation and (b) stretching separation.

on the observed collision dynamics, however, the rotated view here (Fig. 9, right) is used to develop a model that accounts for the actual interaction of the droplets on the impact plane. When  $B = 0$ , the entire mass of the two droplets interacts on the impact plane symmetrically. When  $B > 0$ , only a part of the droplet interacts. With the decomposition of the collision motion, the volume of the interacting portion can be calculated from the time integration of the interacting area on the impact plane. Immediately before the two droplets come into contact with each other, the interacting area is zero, as shown in Fig. 9, right. Note that in practice, the two droplets meet each other at a slightly deformed surface due to the cushion effect of the gas film. Figure 25(a) schematically shows the interaction of the droplets at a given moment. The colored regions in the top schematic represent the mass that does not interact. The dashed line represents the surface of the mass passing through the impact plane. The bottom figure highlights the impact plane, with a colored interaction area that has a lens-like shape. Figure 25(b) shows that the

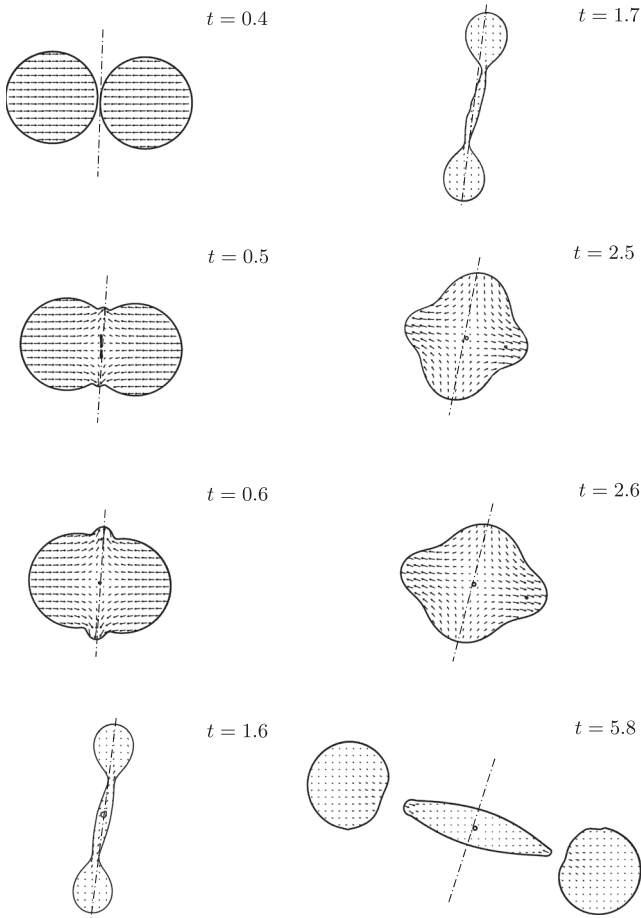


**FIG. 23.** Evolution of droplet shape and velocity vectors during reflexive separation. Tetradecane droplets in nitrogen at 1 atm,  $We = 61.4$ ,  $Re = 296.5$ ,  $B = 0.06$ ,  $D = 336 \mu\text{m}$ ,  $U = 2.48 \text{ m/s}$ .

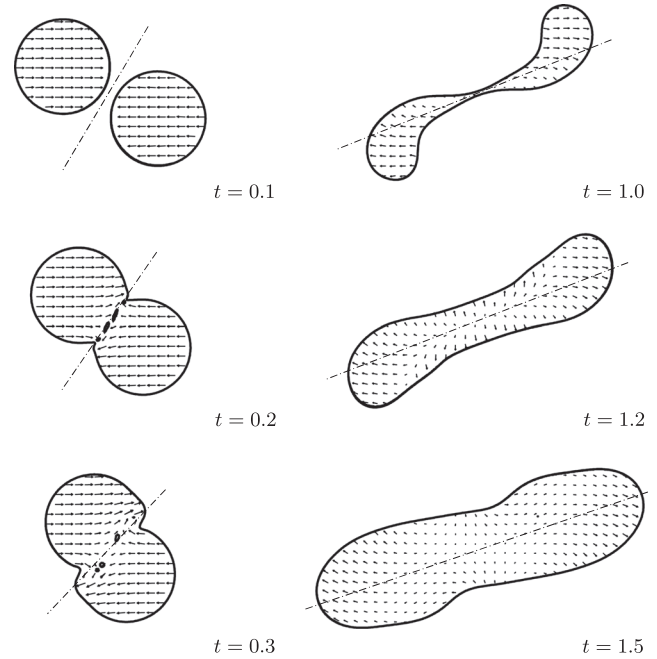


**FIG. 24.** Evolution of shape and velocity vectors during stretching separation. Tetradecane droplets in nitrogen at 1 atm,  $We = 65.1$ ,  $Re = 320.3$ ,  $B = 0.49$ ,  $D = 370 \mu\text{m}$ ,  $U = 2.43 \text{ m/s}$ .

interaction finishes when the noninteracting portions of the two droplets become tangential to each other.

According to the above geometric understanding of the droplet interaction, the volume of the interacting region can then be obtained by integrating the interacting area. Figure 25(c) highlights the entire interacting region. The interacting portion of each droplet can be divided into left and right parts along line  $CD$ , which represents the path of the collision center during the collision. For the top droplet, the left part is a segment of a sphere, whereas the right part has an irregular geometry. Although the shapes of the two parts are different, however, their volumes are identical. Thus, the volume of the interacting portion for each droplet can be expressed as two times the segment volume. The ratio of the volume of the interacting portion to the total volume of a single droplet can be derived as follows:

$$q = \frac{(2 + B)(1 - B)^2}{2}. \tag{15}$$

The interacting surface area can be calculated by integrating the boundary arc length of the interacting area. The surface area of the interacting portion for each droplet can be expressed as the segment surface area with a height of  $(1 - B)R$ . The ratio of the interacting surface area to that of a single droplet takes the following form:

$$q_s = \frac{1 - B}{2}. \tag{16}$$

#### 4. Mass transfer

Figures 20 and 21 show that the mass of the resulting droplets is equal to the mass of the original droplets. The mass transfer ratio,  $f_a$ , can be defined as the ratio of foreign mass to the total mass of a single droplet after the collision. Note that  $f_a$  is different from the mixing rate, which is the local concentration of one liquid in the combined liquid. For a bouncing outcome,  $f_a = 0$  since there is no contact between the two droplets. For a coalescence outcome,  $f_a = 0.5$  because the resulting droplet consists of equal amounts of original droplets. The rendered evolution of the two separation types of droplet collision (see Figs. 20 and 21) shows that the foreign mass is only a small portion of the total mass. However, the satellite droplets are composed of equal masses of the two parent droplets because the interactions are symmetric. The mass transfer ratio is obtained by applying volumetric integration to only the large droplets after the collision. Figure 26 shows the calculated mass transfer ratio in various regimes. The mass transfer ratio has

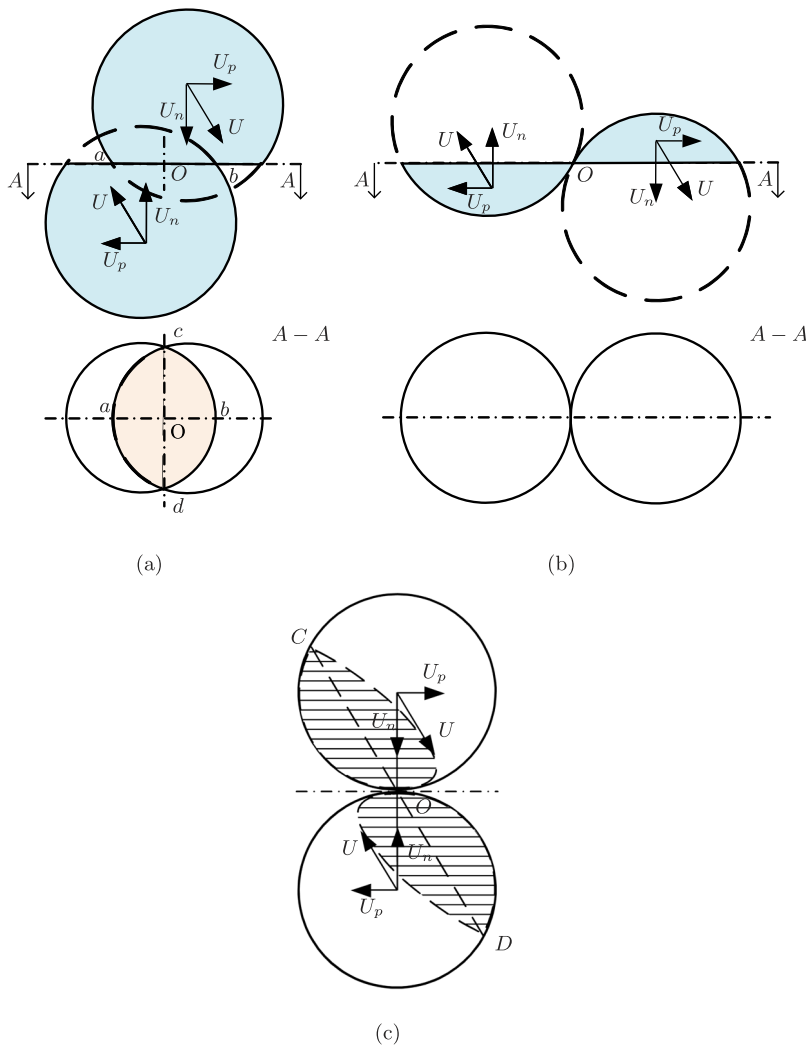


**FIG. 25.** Schematic diagrams for modeling of interacting region. (a) the interaction of the droplets at a given moment; (b) the end of droplet interaction; (c) the entire interacting region.

30 August 2024 21:57:05

a weak dependence on the Weber number, and it is approximately a function of impact factor  $B$ .

Based on this analysis of collision dynamics and the model for droplet interaction during the collision, a theoretical prediction of the mass transfer ratio can be established. To obtain a universal understanding of the mass transfer process, the case with a coalescence outcome (Fig. 19) is analyzed. Figure 27(a) shows the evolution of the cross section from the initial droplet contact ( $t_1$ ) to the maximum deformation ( $t_4$ ). Immediately upon contact at  $t_1$ , the normal motion drives the droplets to interact with each other. Since the forces on the two sides are equal, the mass of the interacting portion cannot pass the impact plane, and the interacting mass is split from the centerline. The noninteracting mass continues to move in the original direction and crosses the impact plane. At maximum deformation ( $t_4$ ), all of the interacting mass is equally split from the centerline and is located on its original side of the impact plane. The noninteracting mass, however, has passed the impact plane and is located on the other side. When the parallel motion is sufficiently

strong to continue the elongation of the combined mass, stretching separation occurs and the combined droplet breaks up at the collision center. If the formation of satellite droplets is neglected, each of the resulting droplets consists of the noninteracting mass and half of the interacting mass of the original droplet. However, if the parallel motion is not sufficiently strong, the surface tension pulls back the elongated mass and a reverse normal motion takes place along the impact plane, as shown in Fig. 27(b). If the reverse normal motion is sufficiently strong, reflexive separation occurs and the combined droplet breaks at the collision center. Each of the resulting droplets then consists of the interacting mass of the original droplet.

Based on the geometric distribution of the interacting portion in Fig. 25(c), the relocation of the mass during the collision is obtained in Fig. 28. In stretching separation, the combined droplet eventually breaks at point O. Four portions,  $a$ ,  $B$ ,  $c$ , and  $d$ , can be divided by line CD, which is the path of O, as shown in Fig. 28(a). One resulting droplet consists of  $a$  and  $B$ , while the other droplet

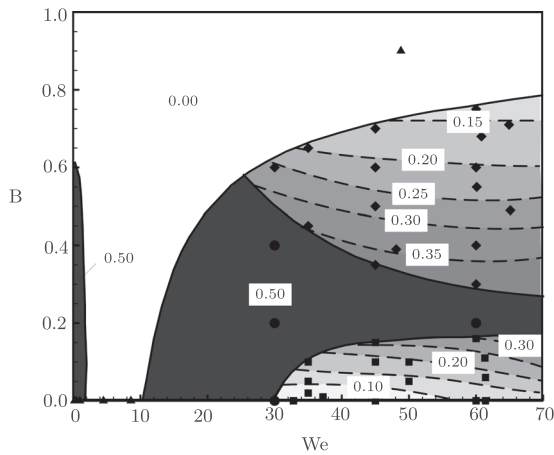


**FIG. 26.** Contour of mass transfer ratio in the collision regime diagram. The solid boundaries are adapted from Ref. 4 (Reproduced with permission from J. Qian and C. K. Law, “Regimes of coalescence and separation in droplet collision,” *J. Fluid Mech.* **331**, 59 (1997). Copyright 1998 Cambridge University Press).

consists of *c* and *d*. Since the volume of *a* and *d* is one half of the interacting portion, the mass transfer ratio for stretching separation can be expressed as follows:

$$f_a^s = q/2 = \frac{(2+B)(1-B)^2}{4}. \tag{17}$$

During reflexive separation, after the interacting mass returns to its original side, the combined droplet breaks at the impact plane. The four portions *e*, *f*, *g*, and *h* can be divided by the boundary of the impacted mass, as shown in Fig. 28(b). The resulting droplets are composed of *e* and *g*, and *f* and *h*. The mass transfer ratio in the reflexive separation can be expressed as follows:

$$f_a^r = 1 - q = \frac{2 - (2+B)(1-B)^2}{2}. \tag{18}$$

Figure 29 shows good consistency between the numerically calculated and the theoretically predicted [Eq. (18)] mass transfer ratio over an impact factor range of  $B = 0-1.0$ .

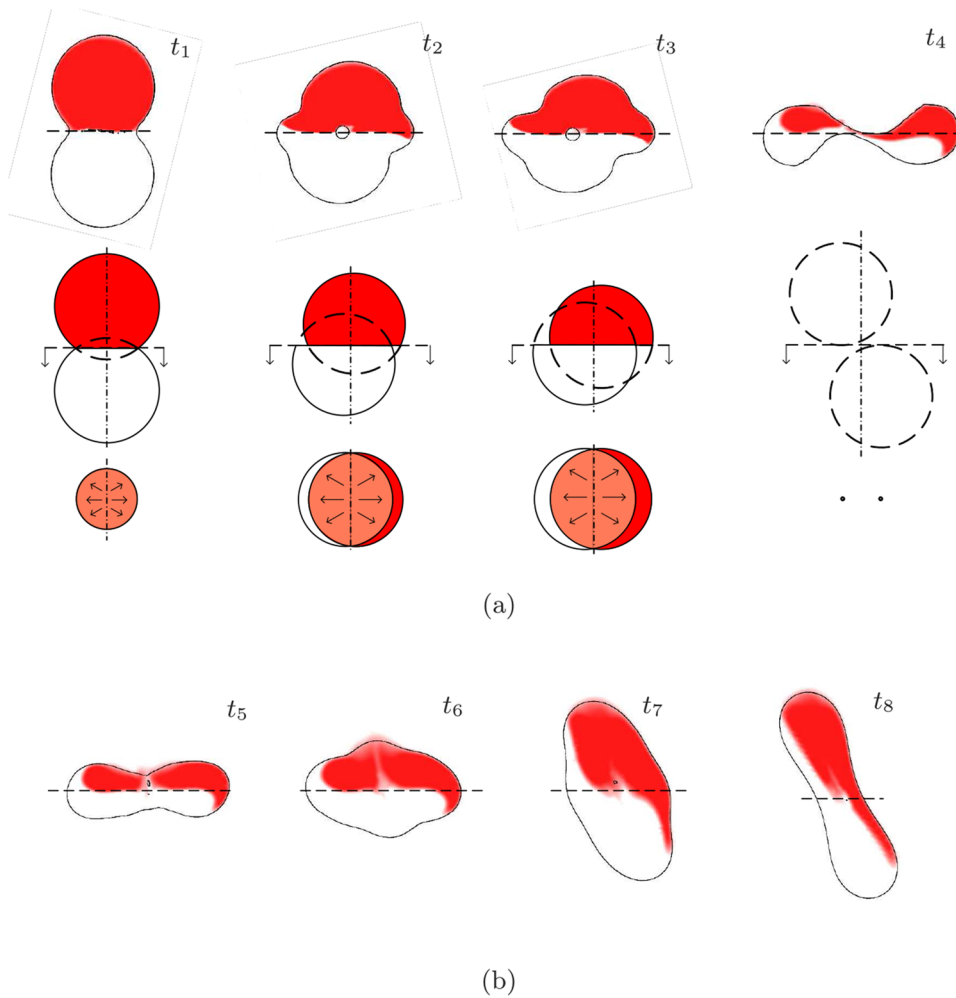


**FIG. 27.** Mass transfer during droplet collision with off-center coalescence. (a) The evolution of the cross-section from the initial droplet contact to the maximum deformation; (b) the evolution of the cross-section during recovery from the maximum deformation.

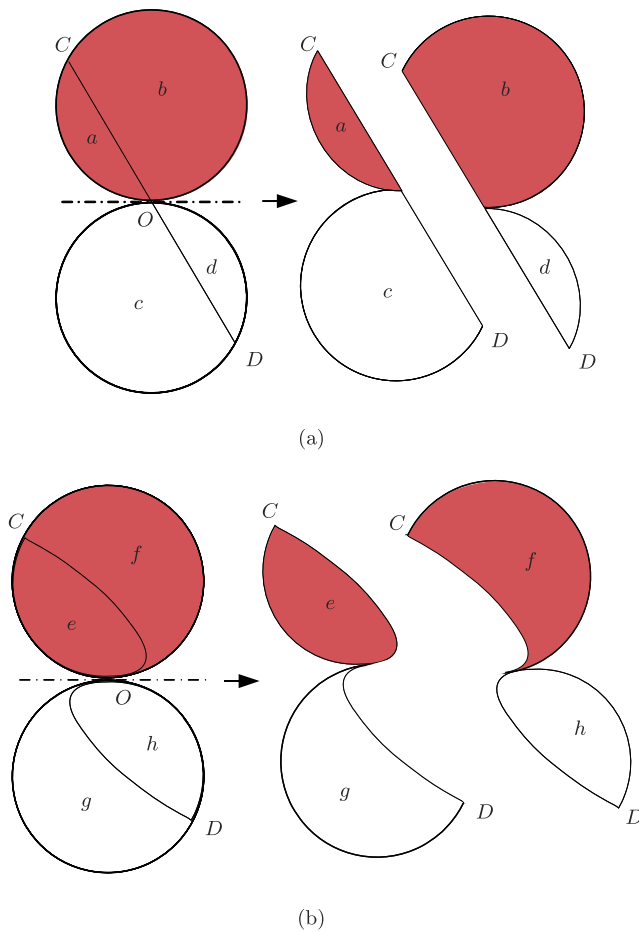


FIG. 28. Divided portions of separation outcome for prediction of mass transfer ratio. (a) Stretching separation; (b) reflexive separation.

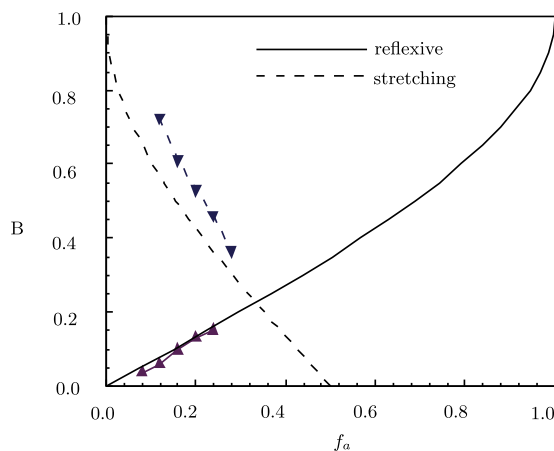


FIG. 29. Calculated and predicted mass transfer ratios for reflexive and stretching separations. ▲, ▼ numerical calculation; —, - - theoretical prediction.

#### IV. CONCLUSIONS

Binary droplet collision, which plays an important role in dense spray dynamics, was studied systematically by means of direct numerical simulations. The formulation is based on complete conservation equations in the continuum mechanics regime with minimal modeling uncertainties. A unified numerical framework that combines an AMR algorithm and a VOF interface tracking technique was developed and implemented to treat the multiscale flow physics of droplet collision. The smallest numerical grid is  $\sim 10$  nm, or on the order of  $10^{-5}$  times the initial droplet diameter, which is sufficient to resolve the near-field droplet dynamics during the collision. A comprehensive parametric study was conducted in terms of Weber number and impact factor to identify the regimes of bouncing, coalescence, reflexive separation, and stretching separation. A visualization technique using the ray-tracing methodology was also developed to gain photorealistic insight into the detailed physics. The nonmonotonic coalescence–bouncing–coalescence transition of the head-on collision was explored. Cases with higher Weber numbers were investigated by analyzing the overall energy budget and the interfacial evolution. In addition, the mass transfer during droplet collision was examined by using a dye as a passive scalar in numerical simulations. Analytical models were developed to predict the interacting volume and surface area during the collision. The mass transfer ratio after the collision was also analyzed to elucidate the dominant physics. Good consistency with the numerical results was obtained.

#### ACKNOWLEDGMENTS

This work was sponsored by the National Natural Science Foundation of China (Grant No. 11772343), the United States Army Research Office under the Multi-University Research Initiative (Contract No. W911NF-08-1-0124), and the Beijing Institute of Technology Research Fund Program for Young Scholars. Support and encouragement from Dr. Ralph Anthenien are gratefully acknowledged. The authors specially thank Dr. Stéphane Popinet for allowing us to use his work on the VOF and AMR algorithms.

#### DATA AVAILABILITY

The data that support the findings of this study are available from the corresponding author upon reasonable request.

#### REFERENCES

- N. Ashgriz and J. Y. Poo, “Coalescence and separation in binary collisions of liquid drops,” *J. Fluid Mech.* **221**, 183 (1990).
- N. Roth, C. Rabe, B. Weigand, F. Feuillebois, and J. Malet, “Droplet collision outcomes at high Weber number,” in *Proceedings 21st Conference Institute for Liquid Atomization and Spray Systems (ILASS), Mugla, Turkey, 2007* (ILASS, Mugla, Turkey, 2007), pp. 10–12.
- K.-L. Pan, P.-C. Chou, and Y.-J. Tseng, “Binary droplet collision at high Weber number,” *Phys. Rev. E* **80**, 036301 (2009).
- J. Qian and C. K. Law, “Regimes of coalescence and separation in droplet collision,” *J. Fluid Mech.* **331**, 59 (1997).
- G. H. Ko and H. S. Ryou, “Modeling of droplet collision-induced breakup process,” *Int. J. Multiphase Flow* **31**, 723 (2005).
- A. Munnannur and R. D. Reitz, “A new predictive model for fragmenting and non-fragmenting binary droplet collisions,” *Int. J. Multiphase Flow* **33**, 873 (2007).

- <sup>7</sup>Y. J. Jiang, A. Umemura, and C. K. Law, "An experimental investigation on the collision behaviour of hydrocarbon droplets," *J. Fluid Mech.* **234**, 171 (1992).
- <sup>8</sup>K. Willis and M. Orme, "Binary droplet collisions in a vacuum environment: An experimental investigation of the role of viscosity," *Exp. Fluids* **34**, 28 (2003).
- <sup>9</sup>M. Dai and D. P. Schmidt, "Numerical simulation of head-on droplet collision: Effect of viscosity on maximum deformation," *Phys. Fluids* **17**, 041701 (2005).
- <sup>10</sup>C. Gotaas, P. Havelka, H. A. Jakobsen, H. F. Svendsen, M. Hase, N. Roth, and B. Weigand, "Effect of viscosity on droplet-droplet collision outcome: Experimental study and numerical comparison," *Phys. Fluids* **19**, 102106 (2007).
- <sup>11</sup>K. G. Krishnan and E. Loth, "Effects of gas and droplet characteristics on drop-drop collision outcome regimes," *Int. J. Multiphase Flow* **77**, 171 (2015).
- <sup>12</sup>M. Sommerfeld and M. Kuschel, "Modelling droplet collision outcomes for different substances and viscosities," *Exp. Fluids* **57**, 187 (2016).
- <sup>13</sup>J.-P. Estrade, H. Carentz, G. Lavergne, and Y. Biscos, "Experimental investigation of dynamic binary collision of ethanol droplets—A model for droplet coalescence and bouncing," *Int. J. Heat Fluid Flow* **20**, 486 (1999).
- <sup>14</sup>I. V. Roisman, "Dynamics of inertia dominated binary drop collisions," *Phys. Fluids* **16**, 3438 (2004).
- <sup>15</sup>K.-L. Pan and I. V. Roisman, "Note on "Dynamics of inertia dominated binary drop collisions" [Phys. Fluids 16, 3438 (2004)]," *Phys. Fluids* **21**, 022101 (2009).
- <sup>16</sup>P. Zhang and C. K. Law, "An analysis of head-on droplet collision with large deformation in gaseous medium," *Phys. Fluids* **23**, 042102 (2011).
- <sup>17</sup>M. R. Nobari, Y. J. Jan, and G. Tryggvason, "Head-on collision of drops—A numerical investigation," *Phys. Fluids* **8**, 29 (1996).
- <sup>18</sup>K.-L. Pan, C. K. Law, and B. Zhou, "Experimental and mechanistic description of merging and bouncing in head-on binary droplet collision," *J. Appl. Phys.* **103**, 064901 (2008).
- <sup>19</sup>X. Jiang and A. J. James, "Numerical simulation of the head-on collision of two equal-sized drops with van der Waals forces," *J. Eng. Math.* **59**, 99 (2007).
- <sup>20</sup>Y. Yoon, F. Baldessari, H. D. Cenicerros, and L. G. Leal, "Coalescence of two equal-sized deformable drops in an axisymmetric flow," *Phys. Fluids* **19**, 102102 (2007).
- <sup>21</sup>M. Kwakkel, W.-P. Breugem, and B. J. Boersma, "Extension of a CLSVOF method for droplet-laden flows with a coalescence/breakup model," *J. Comput. Phys.* **253**, 166 (2013).
- <sup>22</sup>A. H. Rajkotwala, H. Mirsandi, E. A. J. F. Peters, M. W. Baltussen, C. W. M. Van der Geld, J. G. M. Kuerten, and J. A. M. Kuipers, "Extension of local front reconstruction method with controlled coalescence model," *Phys. Fluids* **30**, 022102 (2018).
- <sup>23</sup>L. R. Mason, G. W. Stevens, and D. J. Harvie, "Multi-scale volume of fluid modelling of droplet coalescence," in *9th International Conference on CFD in the Minerals and Process Industries, Melbourne, Australia, 10-12 December 2012* (CSIRO, Canberra, Australia, 2012).
- <sup>24</sup>N. M. Musehane, O. F. Oxtoby, and B. D. Reddy, "Multi-scale simulation of droplet-droplet interaction and coalescence," *J. Comput. Phys.* **373**, 924 (2018).
- <sup>25</sup>X. Chen and V. Yang, "Thickness-based adaptive mesh refinement methods for multi-phase flow simulations with thin regions," *J. Comput. Phys.* **269**, 22 (2014).
- <sup>26</sup>T. Inamuro, S. Tajima, and F. Ogino, "Lattice Boltzmann simulation of droplet collision dynamics," *Int. J. Heat Mass Transfer* **47**, 4649 (2004).
- <sup>27</sup>Y. Pan and K. Suga, "Numerical simulation of binary liquid droplet collision," *Phys. Fluids* **17**, 082105 (2005).
- <sup>28</sup>Z. Sun, G. Xi, and X. Chen, "Mechanism study of deformation and mass transfer for binary droplet collisions with particle method," *Phys. Fluids* **21**, 032106 (2009).
- <sup>29</sup>G. Finotello, J. T. Padding, N. G. Deen, A. Jongsma, F. Innings, and J. A. M. Kuipers, "Effect of viscosity on droplet-droplet collisional interaction," *Phys. Fluids* **29**, 067102 (2017).
- <sup>30</sup>S. Popinet, "An accurate adaptive solver for surface-tension-driven interfacial flows," *J. Comput. Phys.* **228**, 5838 (2009).
- <sup>31</sup>J. U. Brackbill, D. B. Kothe, and C. Zemach, "A continuum method for modeling surface tension," *J. Comput. Phys.* **100**, 335 (1992).
- <sup>32</sup>S. Popinet and S. Zaleski, "A front-tracking algorithm for accurate representation of surface tension," *Int. J. Numer. Methods Fluids* **30**, 775 (1999).
- <sup>33</sup>X. Chen, D. Ma, V. Yang, and S. Popinet, "High-fidelity simulations of impinging jet atomization," *Atomization Sprays* **23**, 1079–1101 (2013).
- <sup>34</sup>X. Chen, Y. Song, D. Li, and G. Hu, "Deformation and interaction of droplet pairs in a microchannel under ac electric fields," *Phys. Rev. Appl.* **4**, 024005 (2015).
- <sup>35</sup>B. J. Hamrock, S. R. Schmid, and B. O. Jacobson, *Fundamentals of Fluid Film Lubrication* (CRC Press, 2004).
- <sup>36</sup>H. Lamb and S. H. Lamb, *Hydrodynamics* (Cambridge University Press, 1997).
- <sup>37</sup>S. Yamakita, Y. Matsui, and S. Shiokawa, "New method for measurement of contact angle (droplet free vibration frequency method)," *Jpn. J. Appl. Phys., Part 1* **38**, 3127 (1999).
- <sup>38</sup>C. He, X. Xia, and P. Zhang, "Vortex-dynamical implications of nonmonotonic viscous dissipation of off-center droplet bouncing," *Phys. Fluids* **32**, 032004 (2020).
- <sup>39</sup>C. He, X. Xia, and P. Zhang, "Non-monotonic viscous dissipation of bouncing droplets undergoing off-center collision," *Phys. Fluids* **31**, 052004 (2019).
- <sup>40</sup>C. Hu, S. Xia, C. Li, and G. Wu, "Three-dimensional numerical investigation and modeling of binary alumina droplet collisions," *Int. J. Heat Mass Transfer* **113**, 569 (2017).
- <sup>41</sup>H. A. Stone, B. J. Bentley, and L. G. Leal, "An experimental study of transient effects in the breakup of viscous drops," *J. Fluid Mech.* **173**, 131 (1986).
- <sup>42</sup>F. M. White, *Viscous Fluid Flow* (McGraw-Hill, Inc., 1991).